

## Transported filtered density function in self-adaptive turbulence eddy simulation

Yuxuan Chen <sup>1</sup>, Tianwei Yang <sup>2</sup>, Hua Zhou,<sup>1</sup> Xingsi Han,<sup>3</sup> and Zhuyin Ren <sup>1,\*</sup>

<sup>1</sup>*Institute for Aero Engine, Tsinghua University, Beijing 100084, China*

<sup>2</sup>*National Research Center for Information Science and Technology, Tsinghua University, Beijing 100084, China*

<sup>3</sup>*Department of Energy and Power Engineering, Nanjing University of Aeronautics and Astronautics, Nanjing 210000, China*



(Received 4 October 2023; accepted 29 January 2024; published 4 March 2024)

The filtered density function (FDF) in the context of large eddy simulation (LES) has demonstrated its unique strength in predicting complex turbulent reacting flows. However, the high computational cost of FDF-LES may hinder its application in industrial configurations. The combination of FDF with the hybrid Reynolds-averaged Navier–Stokes (RANS)-LES method can potentially provide an effective means to significantly reduce computational cost while maintaining accuracy. In this work, the FDF method within the framework of self-adaptive turbulence eddy simulation (SATES), a hybrid RANS-LES approach, is formulated. The focus is on ensuring consistency in both definition and scalar-mixing modeling. The filtered density function in SATES-FDF can be interpreted as the spatial filtering density function under either RANS or LES filtering scale, depending on the local turbulence integral scale and grid resolution. The inconsistency of scalar-mixing rate modeling between RANS mode and LES mode in SATES-FDF is revealed. The general modeling criteria for modeling consistency of scalar-mixing rate are formulated in the context of SATES. A scalar-mixing rate model is then proposed through dimensional analysis, which utilizes a hybrid length scale to meet the criteria and achieve the consistency. The SATES-FDF approach is demonstrated in the simulations of standard turbulent premixed swirling burner TECFLAM, in which the  $k-\omega$  shear stress transport model is adopted for the base model of SATES. With the consistency issue being resolved, it is shown that this mixing-frequency model achieves better overall agreement with experimental data than the classic models in standalone RANS or LES context in terms of reproducing the swirling flow and related flame characteristics, demonstrating its potential for practical combustor configurations. Finally, H equivalence is employed to extend SATES-FDF to more several hybrid RANS-LES frameworks, such that a unified framework for FDF in conjunction with hybrid RANS-LES method is established.

DOI: [10.1103/PhysRevFluids.9.033201](https://doi.org/10.1103/PhysRevFluids.9.033201)

### I. INTRODUCTION

Large eddy simulation (LES), which can effectively resolve large-scale turbulent motions, has been applied in many laboratory-scale flames [1–11] and even industrial-scale combustion chambers [12–15]. However, LES could be computationally expensive, especially for wall-bounded turbulent flows in industrial applications [16]. It requires, therefore, a balance between the accuracy of physical modeling and the computational cost, particularly for wall-bounded flows. Recently, hybrid

\*Corresponding author: zhuyinren@tsinghua.edu.cn

Reynolds-averaged Navier–Stokes (RANS)-LES method (HRLM) [17] has gained popularity for its high accuracy and low computational cost, and these hybrid techniques are designed to operate in LES mode in regions where transient effects are strong and in RANS mode in other regions to save computational cost. A number of strategies for combining RANS and LES equations have been proposed thus far; for instance, detached eddy simulation (DES) [18], partially averaged Navier-Stokes (PANS) [19–21], partially integrated transport model (PITM) [22], and self-adaptive turbulence eddy simulation (SATES) [23,24]. These methods, also called adaptive turbulence model, focus on the utilization of a unified modeling framework that encompasses the three primary computational modes: RANS, LES, and direct numerical simulation (DNS), and facilitates the seamless transition between RANS, LES, and DNS depending on local turbulent scales and computational grid resolution. SATES, developed from very large eddy simulation (VLES) proposed by Speziale [25], is a representative of such hybrid RANS-LES methods. Its capacity to achieve both efficiency and accuracy for highly turbulent flows has been demonstrated in classical isothermal turbulent-flow cases [26] as well as in complex strong swirling flow [27]. However, the utilization of hybrid RANS-LES method in the presence of reaction, i.e., for complex turbulent flames, has received less attention [28]. One of the primary reasons that hinders utilization is that the different modes in hybrid RANS-LES method could lead to modeling inconsistency of some combustion models that have different modeling strategies in RANS or LES context.

Transported filtered density function (FDF), which closes the mean chemical source term without any approximation [29–33], has shown great potential for predicting near-limit flame characteristics and emissions in laboratory-scale flames (jet, swirl, layered, nonpremixed, premixed, etc.) [3–6,11] and turbulent flames in industrial devices [13]. However, one of the great challenges for the one-point, one-time FDF representation is the conditional molecular-diffusion term which requires the closure by the micromixing model [34–38]. As the key component for a micromixing model, the scalar-mixing timescale depends on the level of turbulence closure. Specifically, with the constant scalar-mechanical ratio model, the scalar-mixing timescale is modeled as  $\tau_M = \frac{\tau_{\text{turb}}}{C_M}$  [31,32], where  $C_M$  is the mixing-rate parameter and  $\tau_{\text{turb}}$  is the (subgrid) turbulent timescale. In RANS concept,  $\tau_{\text{turb}} \sim \omega^{-1}$ , which is grid independent with  $\omega$  being specific dissipation, while in LES concept,  $\tau_{\text{turb}} \sim \Delta^2/(\nu_t + \nu)$ , which is grid dependent with  $\nu_t$ ,  $\nu$ , and  $\Delta$ , respectively, being turbulent-laminar viscosity and filter size. In the framework of hybrid RANS-LES method, with the change of local turbulent scales and grid resolution, the closure for local turbulence could transition between LES and RANS. Challenges remain on ensuring the consistent scalar-mixing timescale modeling when transitioning between RANS and LES modes.

This study aims at formulating the FDF method in the context of hybrid RANS-LES method, focusing on the consistency in the definition and scalar-mixing modeling. The SATES is first employed as an example to demonstrate the concepts and methodology. The applications of SATES-FDF are then demonstrated for turbulent swirling premixed flames with bluff body, i.e., TECFLAM [39–41], which has been extensively studied [42–44]. Finally, H equivalence is employed to extend SATES-FDF to general hybrid RANS-LES method in the Appendix.

## II. METHODOLOGY

### A. Self-adaptive turbulence eddy simulation method

The SATES method [23,24] is formulated based on the VLES method originally developed by Speziale [25]. In the present SATES modeling framework, the Navier-Stokes equations for low-Mach Newtonian fluids are solved,

$$\frac{\partial \bar{\rho}}{\partial t} + \frac{\partial}{\partial x_j}(\bar{\rho} \tilde{u}_j) = 0, \quad (1)$$

$$\frac{\partial}{\partial t}(\bar{\rho} \tilde{u}_i) + \frac{\partial}{\partial x_j}(\bar{\rho} \tilde{u}_i \tilde{u}_j) = -\frac{\partial \bar{p}}{\partial x_i} + \frac{\partial}{\partial x_j} \left[ (\mu + \mu_i^{\text{sub}}) \left( \frac{\partial \tilde{u}_i}{\partial x_j} + \frac{\partial \tilde{u}_j}{\partial x_i} \right) \right], \quad (2)$$

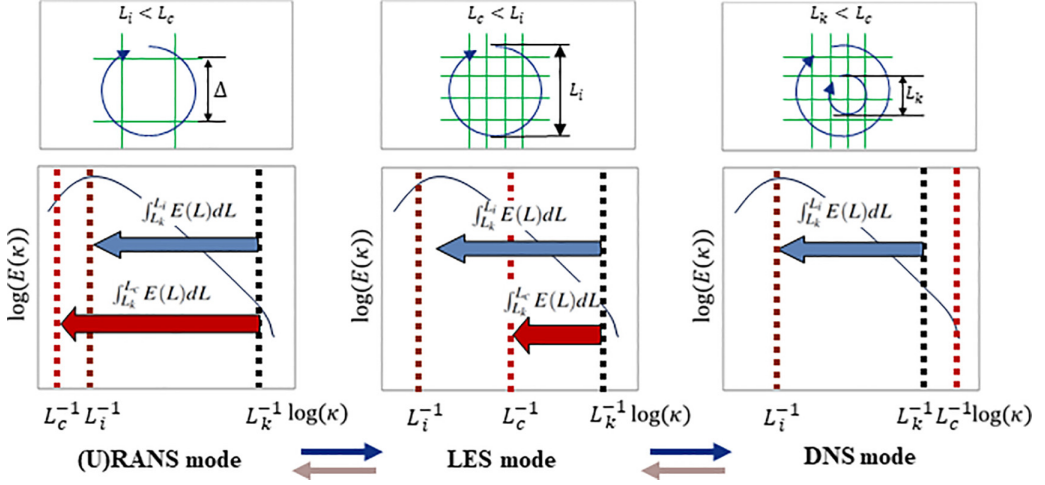


FIG. 1. Schematic diagram of the SATES simulation modes with different grid resolution (above); schematic diagram of turbulence energy spectrum corresponding to different SATES modeling modes (below).

where the overbars “-” and “~,” respectively, refer to averaged and Favre-averaged variables. In RANS mode, it refers to ensemble-averaged variables, while in LES mode, it refers to spatially averaged variables, with the fluid density  $\rho$ , the velocity components  $u_i$ , the pressure  $p$ , the laminar viscosity  $\mu$ , and the turbulent viscosity  $\mu_t^{\text{sub}}$  to be modeled. By introducing the resolution control function  $F_r$ , the unresolved turbulent viscosity  $\mu_t^{\text{sub}}$  can be modeled as

$$\mu_t^{\text{sub}} = F_r \mu_t^{\text{RANS}}, \quad (3)$$

with  $\mu_t^{\text{RANS}}$  being the turbulent viscosity in RANS framework, such that a set of RANS turbulence model can serve as the basis in SATES. In this study, the  $k-\omega$  shear stress transport (SST) model is employed as an example for illustration purpose, in which the transport equations of turbulence kinetic energy  $k$  and the specific dissipation  $\omega$  are

$$\frac{\partial \bar{\rho} k}{\partial t} + \frac{\partial \bar{\rho} \tilde{u}_j k}{\partial x_j} = \bar{\rho} P_k - \beta^* \bar{\rho} k \omega + \frac{\partial}{\partial x_j} \left[ \left( \mu + \frac{\mu_t^{\text{sub}}}{\sigma_k} \right) \frac{\partial k}{\partial x_j} \right], \quad (4)$$

$$\frac{\partial \bar{\rho} \omega}{\partial t} + \frac{\partial \bar{\rho} \omega \tilde{u}_j}{\partial x_j} = \gamma \frac{\omega}{k} \bar{\rho} P_k - \beta_1 \bar{\rho} \omega^2 + \frac{\partial}{\partial x_j} \left[ \left( \mu + \frac{\mu_t^{\text{sub}}}{\sigma_\omega} \right) \frac{\partial \omega}{\partial x_j} \right] + 2 \bar{\rho} (1 - F_1) \sigma_{\omega 2} \frac{1}{\omega} \frac{\partial k}{\partial x_j} \frac{\partial \omega}{\partial x_j}, \quad (5)$$

where  $P_k = \frac{2\mu_t^{\text{sub}} S_{ij} S_{ij}}{\bar{\rho}}$ , where  $S_{ij} = \frac{1}{2} \left( \frac{\partial u_i}{\partial x_j} + \frac{\partial u_j}{\partial x_i} \right)$  is the production term, the model constants are  $\sigma_k = 2$ ,  $\alpha = 2$ ;  $\sigma_{\omega 2} = 0.856$ ;  $\beta_1 = 3/40$ ;  $\gamma = 5/9$ ; and  $F_1$  is a function of  $k$ ,  $\omega$ ,  $\mu$ , and the distance to the wall  $d_w$  as described in Ref. [48]. The turbulent viscosity  $\mu_t^{\text{RANS}}$  is given by

$$\mu_t^{\text{RANS}} = \bar{\rho} \frac{k}{\omega}. \quad (6)$$

For the modeling of resolution control function  $F_r$ , Fig. 1 illustrates the different turbulent modeling modes of SATES with various grid resolution. The specific modes are dynamically determined according to the relative size between local grid resolution and turbulent scales. Specifically, the SATES works in a LES mode locally if the local grid resolution is sufficient to capture most turbulent kinetic energy, i.e., over 80% of the turbulent kinetic energy is resolved, and works in a VLES mode if only a few large turbulent vortices can be captured and less than 80% of the turbulence energy is

resolved, and works in RANS mode if the local grid resolution is so low that even turbulent vortices at the integral length scale cannot be captured and all turbulence energy must be modeled. One key aspect of SATES is how to trigger the mode transition such that the transition occurs seamlessly and efficiently between the RANS and LES modes. This is crucial for maintaining the accuracy and reliability of the simulation.

Han *et al.* [23,24] constructed the resolution control function  $F_r$  as a trigger, which incorporates the cutoff length scale,  $L_c$ , integral length scale,  $L_i$ , and Kolmogorov length scale,  $L_k$ . As illustrated in Fig. 1, from the energy-spectrum perspective, the corresponding SATES mode is determined by wave numbers,

$$(\kappa_i, \kappa_c, \kappa_k) = 2\pi(L_i^{-1}, L_c^{-1}, L_k^{-1}), \quad (7)$$

where  $\kappa_i$ ,  $\kappa_c$ , and  $\kappa_k$  are the wave numbers corresponding to the integral, cutoff, and Kolmogorov length scales, respectively. For the cutoff wave number  $\kappa_c$  falling within the inertial subrange, the energy spectrum adheres to the well-known  $-5/3$  law as

$$E(\kappa) \approx C_k \varepsilon^{2/3} \kappa^{-(5/3)}, \quad \kappa_i \leq \kappa_c \leq \kappa_k. \quad (8)$$

The total turbulence kinetic energy (TKE) can be estimated via  $\int_{L_k}^{L_i} E(L)dL \approx [1 - \exp(-\beta L_i/L_k)]^n$ , while the unresolved TKE can be approximated with  $\int_{L_k}^{L_c} E(L)dL \approx [1 - \exp(-\beta L_c/L_k)]^n$ , where  $\beta \sim O(10^{-3})$  and  $n \sim O(1)$ . Based on Pope's theory [45], for LES mode, the unresolved TKE proportion,  $\int_{L_k}^{L_c} E(L)dL$ , needs to be below 20% of the total TKE. The SATES transfers to VLES mode locally if the cutoff wave number  $\kappa_c$  is in the inertial subrange but has an unresolved TKE being larger than 20% of the total TKE. The SATES transfers to RANS mode locally if the cutoff wave number  $\kappa_c$  is below the integral wave number  $\kappa_i$ , i.e., outside the inertial subrange, the total TKE has to be modeled.

Following the generic form of the resolution control by Hsieh *et al.* [46],

$$f_r = \frac{\int_{L_k}^{L_c} E(L)dL}{\int_{L_k}^{L_i} E(L)dL}, \quad (9)$$

the resolution control function is defined as [23,24]

$$F_r = \min[1.0, f_r^2] = \min\left[1.0, \left(\frac{1.0 - \exp(-\beta L_c/L_k)}{1.0 - \exp(-\beta L_i/L_k)}\right)^2\right], \quad (10)$$

with the three length scales being determined as

$$L_c = C_{VLES} \Delta; \quad L_i = k^{1/2}/(\beta^* \omega); \quad L_k = \nu^{3/4}/(\beta^* k \omega)^{1/4}, \quad (11)$$

where  $k$  and  $\omega$  are, respectively, the turbulence kinetic energy and the specific dissipation, the model constants  $\beta = 0.002$ , and  $\beta^* = 0.09$ . Note that the parameter  $C_{VLES}$  is related to the Smagorinsky constant  $C_S$  as  $C_{VLES} = \sqrt{0.3} C_S / \beta^*$ , which could be obtained by assuming that the RANS model is identical to the standard Smagorinsky LES model [47] when  $F_r$  is exactly 1 for continuous transition between RANS mode and LES mode. When  $C_{VLES} = 0.12$ ,  $C_S \approx 0.02$ , and when  $C_{VLES} = 0.61$ ,  $C_S \approx 0.1$  [23].

The adaptive change of  $F_r$  between 0 and 1 with local mesh resolution and local turbulent scale allows the SATES method to cover RANS, VLES, LES, and correctly approach DNS within one modeling framework. In specific cases, when the mesh scale is incapable of resolving the largest turbulence scale, i.e.,  $F_r$  approaches 1, a RANS-like modeling is applied; when the mesh resolution

can resolve a majority of turbulent scales, i.e.,  $F_r$  is considerably lower than 1, a LES-like modeling is used; when  $F_r$  approaches 0, indicating the mesh scale can resolve the minimum turbulence scale (Kolmogorov length scale), the calculation approaches the DNS limit.

## B. Transported FDF in SATES

### 1. FDF concepts in SATES

The FDF method is an approach that provides the closure for subgrid-scale quantities in a probabilistic manner. The advantage of this methodology is obvious, i.e., if the FDF of a transport quantity is known, all of its statistical moments are readily determined. The joint FDF of composition is defined as  $f_{\text{FDF}}(\Psi, \mathbf{x}, t) = \langle \delta(\phi(\mathbf{x}, t) - \Psi) \rangle_{\Delta_G} = \int G(\mathbf{r}, \Delta_G) \delta(\phi(\mathbf{x} + \mathbf{r}, t) - \Psi) d\mathbf{r}$ , where  $\langle \bullet \rangle_{\Delta_G}$  represents spatial filtering with the filter size  $\Delta_G$ , and  $G(\mathbf{r}, \Delta_G)$  is a homogeneous filter function which satisfies  $\int G(\mathbf{r}, \Delta_G) d\mathbf{r} = 1$ ,  $G(\mathbf{r}, \Delta_G) = G(-\mathbf{r}, \Delta_G)$ , and all the moments  $\int \mathbf{r}^m G(\mathbf{r}, \Delta_G) d\mathbf{r}$  should exist for  $m \geq 0$  [33]. Given the FDF of composition, the filtered quantity of any variable  $Q(\mathbf{x}, t) = Q(\phi)$  with respect to component  $\phi$  can be obtained by  $\langle Q(\mathbf{x}, t) \rangle_{\Delta_G} = \int G(\mathbf{r}, \Delta_G) Q(\mathbf{x} + \mathbf{r}, t) d\mathbf{r}$ .

In the framework of SATES, two modes for turbulence closure, i.e., RANS and LES, are involved. RANS and LES are conceptually deterministic and stochastic, respectively. However, it is worth appreciating that the concept of RANS and LES can be interpreted from various perspectives. For example, it has been argued by Perot [49] that while the RANS equations can be derived from the assumption of ensemble averaging and the LES equations from filtering operations, these assumptions are overly restrictive and neither system must be derived with those assumptions. The key idea of the SATES is to interpret Reynolds averaging as the spatial filtering with a considerably larger filter width. In this sense, SATES ensures the consistency between RANS and LES by employing the identical transport equations but adapting different filter width according to the local turbulence and grid resolution.

Therefore, the concept of FDF in RANS and LES can essentially be interpreted as filtered density function with the filter size based on integral length scale and computational cell size, respectively, i.e.,  $L_c = C_{\text{VLES}} \Delta$ ;  $L_i = k^{1/2}/(\beta^* \omega)$ . Given two linear and constant preserving filters ( $G_1$  and  $G_2$ ) with the filter size of  $L_i = k^{1/2}/(\beta^* \omega)$  and  $L_c = C_{\text{VLES}} \Delta$ . The filter function and filter size satisfy the following formulation [50]:

$$L_i^2 = \int \mathbf{r}^2 G_1(\mathbf{r}, L_i) d\mathbf{r}, \quad (12)$$

$$L_c^2 = \int \mathbf{r}^2 G_2(\mathbf{r}, L_c) d\mathbf{r}. \quad (13)$$

An additive filter function ( $G_3$ ) is defined by Germano [50] as

$$G_3(\mathbf{r}, L_{\text{hybrid}}) = \alpha G_1(\mathbf{r}, L_i) + (1 - \alpha) G_2(\mathbf{r}, L_c). \quad (14)$$

Therefore,  $L_{\text{hybrid}}^2 = \alpha L_i^2 + (1 - \alpha) L_c^2$ , where  $\alpha$  is bounded between 0 and 1. For SATES,  $\alpha$  is 0 if  $L_c < L_i$ , and  $\alpha$  is 1 if  $L_c \geq L_i$ ; the former situation corresponds to  $F_r < 1$  as shown in the middle of Fig. 1, while the latter situation corresponds to  $F_r = 1$  as shown in the left of Fig. 1,

$$\alpha = \begin{cases} 0 & \text{if } L_c < L_i \\ 1 & \text{if } L_c \geq L_i \end{cases}. \quad (15)$$

Equations (14) and (15) yield

$$L_{\text{hybrid}} = \min(L_i, L_c), \quad (16)$$

thus,

$$\begin{aligned} \langle Q(\mathbf{x}, t) \rangle_{L_{\text{hybrid}}} &= \int G_3(\mathbf{r}, L_{\text{hybrid}}) Q(\mathbf{x} + \mathbf{r}, t) d\mathbf{r} \\ &= \alpha \int G_1(\mathbf{r}, L_i) Q(\mathbf{x} + \mathbf{r}, t) d\mathbf{r} + (1 - \alpha) \int G_2(\mathbf{r}, L_c) Q(\mathbf{x} + \mathbf{r}, t) d\mathbf{r}. \end{aligned} \quad (17)$$

Finally, Eq. (17) yields

$$\langle Q(\mathbf{x}, t) \rangle_{L_{\text{hybrid}}} = \alpha \langle Q(\mathbf{x}, t) \rangle_{L_i} + (1 - \alpha) \langle Q(\mathbf{x}, t) \rangle_{L_c} = \begin{cases} \langle Q(\mathbf{x}, t) \rangle_{L_c} & \text{if } L_c < L_i \\ \langle Q(\mathbf{x}, t) \rangle_{L_i} & \text{if } L_c \geq L_i \end{cases}. \quad (18)$$

Equation (18) means that the filter size in SATES-FDF takes the minimum of  $L_i$  and  $L_c$ . In RANS mode ( $L_c \geq L_i$ ), the filter size is grid independent. And, if  $L_i$  is large enough and turbulence can be assumed to be homogeneous, from ergodic hypothesis,  $\int G_1(\mathbf{r}, L_i) Q(\mathbf{x} + \mathbf{r}, t) d\mathbf{r} = \langle Q(\mathbf{x}, t) \rangle$ , where  $\langle \bullet \rangle$  means ensemble average and  $f_{\text{PDF}}(\Psi, \mathbf{x}, t)$  is converted to  $f_{\text{PDF}}(\Psi, \mathbf{x}, t) = \langle \delta(\phi(\mathbf{x}, t) - \Psi) \rangle$ , where PDF stands for probability density function. In LES mode ( $L_c < L_i$ ), the filter size is grid dependent, which is similar to the filter size in LES context.

## 2. Monte Carlo particle method

Following the above interpretation of FDF in hybrid RANS-LES method, the Lagrangian Monte Carlo particle algorithm as in LES-FDF can be directly adopted, in which computational particles evolve in physical and composition space according to the following stochastic differential equations:

$$d\mathbf{x}^* = \{ \tilde{\mathbf{u}} + \nabla[(\tilde{\Gamma} + \tilde{\Gamma}_t)\bar{\rho}]/\bar{\rho} \}^* dt + \sqrt{2(\tilde{\Gamma} + \tilde{\Gamma}_t)} d\mathbf{W}^*, \quad (19)$$

$$d\phi^*(t) = \mathbf{M}(\phi^*)dt + \mathbf{S}(\phi^*)dt, \quad (20)$$

where the superscript  $*$  represents a specific property of an individual particle or a value of the SATES field assessed at the location of the particle,  $\tilde{\mathbf{u}}$ ,  $\tilde{\Gamma}$ , and  $\tilde{\Gamma}_t^{\text{sub}}$  are respectively, density-weighted spatial filtered velocity, and molecular and turbulent diffusivity interpolated on the particle locations with a second-order piecewise linear scheme [51].  $d\mathbf{W}^*$  is an independent Wiener increment;  $\mathbf{M}(\phi^*)$  represents the rate of change due to the process of molecular mixing closed by a mixing model. Existing models, such as exchange with the mean (IEM) [34], modified Curl's model (MC) [35], Euclidean minimum spanning tree (EMST) model [36], shadow-position mixing model [52], etc., have the same mixing format in the RANS mode or LES mode and can be directly adopted in SATES. For example, with IEM model [34], the micromixing formulation is

$$\mathbf{M}(\phi^*) = -\Omega_\phi(\phi^* - \tilde{\phi}), \quad (21)$$

where  $\Omega_\phi$  is the scalar-mixing rate, and  $\tilde{\phi}$  denotes the density-weighted spatial filtered scalar-mass fraction. Note that  $\Omega_\phi$ , crucial in FDF simulations of turbulent flames [30–33], is commonly assumed to be proportional to turbulent mixing frequency, i.e.,  $\Omega_\phi = C_\phi \Omega_{\text{turb}}$ . There are two major inconsistencies in modeling  $\Omega_\phi$  between RANS and LES. In RANS,  $\Omega_{\text{turb}} = \frac{\varepsilon}{k} = \beta^* \omega$  is grid independent, whereas  $\Omega_{\text{turb}} = \frac{u_t + v}{\Delta^2}$  is grid dependent in the framework of LES. Second, the reported values of model parameter  $C_\phi$ , depending on both flow conditions and flame structures [53], are very different in the RANS and LES frameworks. For example,  $C_\phi$  commonly varies from 1.0 to 3.0 in RANS [54], but may vary from 5.0 to 50.0 in LES [52,55,56]. In FDF [30–33,57,58], scalar-mixing timescale is identified to be one of the major sources of uncertainty, and the inconsistency in  $C_\phi$  and  $\Omega_{\text{turb}}$  should be properly resolved.

### 3. Consistency in scalar-mixing rate modeling

To resolve the inconsistency in the transition between RANS mode and LES mode [59], the following four modeling criteria in SATES should be satisfied:

- (1) In RANS mode (i.e.,  $F_r = 1$ ), the SATES equations degenerate into RANS equations;  $\Omega_\phi$  is independent of  $\Delta$  and should be modeled as  $\Omega_\phi = \Omega_{\phi_{\text{RANS}}} = C_{\phi_{\text{RANS}}} \Omega_{\text{RANS}} = C_{\phi_{\text{RANS}}} \beta^* \omega$ .
- (2) In LES (and VLES) mode ( $0 < F_r < 1$ ),  $\Omega_\phi$  scales as  $\Omega_\phi = \Omega_{\phi_{\text{LES}}} = C_{\phi_{\text{LES}}} \frac{v_t + \nu}{\Delta^2}$ .
- (3) In DNS mode (i.e.,  $F_r = 0$ ),  $\Omega_\phi$  scales as  $\Omega_\phi = \Omega_{\phi_{\text{DNS}}} = C_{\phi_{\text{LES}}} \frac{\nu}{\Delta^2}$ , with turbulent viscosity vanishing.
- (4) During mode transition (e.g.,  $F_r \rightarrow 0$  or  $F_r \rightarrow 1$ ), the spatial continuity in  $\Omega_\phi$  should be ensured.

Note that existing models in RANS and LES context could not guarantee the above criteria. For example, with the model  $\Omega_\phi = C_\phi \beta^* \omega$ , when  $F_r \rightarrow 0$ ,  $\frac{v_t}{\Delta^2} = \frac{F_r \cdot k}{\omega \Delta^2} = \frac{k}{\omega \Delta^2} \left(\frac{L_c}{L_i}\right)^2 = (\beta^* C_{\text{VLES}})^2 \omega$ , and one has

$$\Omega_\phi \rightarrow \frac{1}{\beta^* C_{\text{VLES}}^2} C_\phi \frac{v_t}{\Delta^2}, \quad (22)$$

which cannot correctly recover the DNS limit. With the model  $\Omega_\phi = C_\phi \frac{v_t + \nu}{\Delta^2}$  being used, when  $F_r = 1$ , it would not be independent with  $\Delta$  in the RANS mode.

To ensure the above four criteria being satisfied, a length scale, which has been introduced in Eq. (16) as the filter size of SATES-FDF, is reintroduced as the characteristic scale in mixing-frequency modeling,

$$L_{\text{hybrid}} = \min(L_i, L_c) = \begin{cases} k^{1/2}/(\beta^* \omega) & \text{if } F_r = 1 \\ C_{\text{VLES}} \Delta & \text{if } 0 \leq F_r < 1 \end{cases}. \quad (23)$$

This mixing-frequency model is formulated as

$$\Omega_\phi = C_{\phi_{\text{hybrid}}} \frac{v_t + \nu}{L_{\text{hybrid}}^2} = \begin{cases} C_{\phi_{\text{RANS}}} \beta^* \omega & \text{if } F_r = 1 \\ C_{\phi_{\text{LES}}} \frac{v_t + \nu}{\Delta^2} & \text{if } 0 \leq F_r < 1 \end{cases}, \quad (24)$$

where the laminar viscosity in RANS mode with  $F_r = 1$  is neglected considering that  $\frac{\nu}{L_i^2} \ll \frac{v_t}{L_i^2}$ . To ensure the spatial continuity from LES mode to RANS mode, i.e., when  $F_r$  is approaching 1 and  $L_i = L_c$ , one should have  $C_{\phi_{\text{RANS}}} \beta^* \omega = C_{\phi_{\text{LES}}} \frac{v_t}{\Delta^2}$ , and thus the model constants  $C_{\phi_{\text{RANS}}}$  and  $C_{\phi_{\text{LES}}}$  should be inherently related to

$$\frac{C_{\phi_{\text{LES}}}}{C_{\phi_{\text{RANS}}}} = \frac{1}{C_{\text{VLES}}^2 \beta^*}. \quad (25)$$

For example, with  $C_{\text{VLES}} = 0.61$ , the ratio is approximately  $\frac{C_{\phi_{\text{LES}}}}{C_{\phi_{\text{RANS}}}} = 30$  to ensure a smooth transition.

### 4. Numerical implementation

The proposed SATES-FDF methods are implemented in an unstructured, based on finite-volume method, parallel and open-source Computational Fluid Dynamics (CFD) software [60]. For the flow fields, a pressure-based solver utilizing the SIMPLEX algorithm [61] is employed for solving the Navier-Stokes equations. This solver is suitable for variable density incompressible flows. An implicit first-order Euler scheme was used for time discretization. A second-order central scheme and a first-order upwind scheme are blending as 90% and 10% was used in velocity-space discretization for the sake of balancing stability and accuracy. Similar operation was done by 80% central scheme and 20% upwind scheme in pressure-space discretization. A pure second-order upwind scheme was used for other scalars, like  $k$  and  $\omega$ .

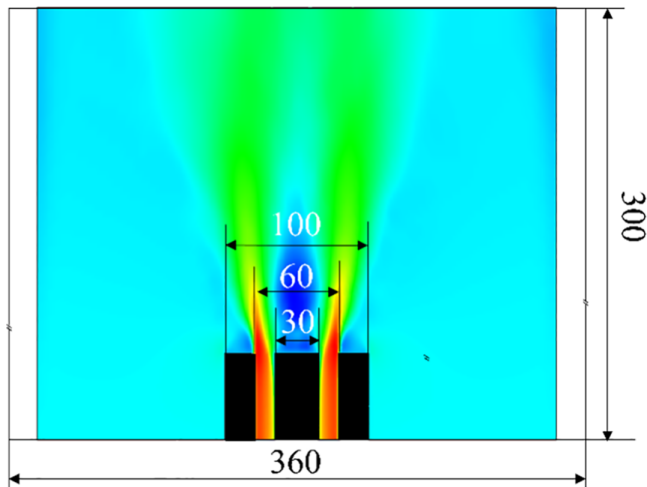


FIG. 2. Sketch of the computational domain with the isothermal simulation results obtained by SATES as background (dimensions in millimeters).

For the sake of simplicity and efficiency, the FDF particle solver currently employs a first-order explicit scheme to transport particles in the physical space. To determine the velocity and relevant quantities governing the movement of particles in Eqs. (19) and (20), linear interpolation of the variables is performed at the particle's initial position during each time step. At the end of a time step, the particle's cell ID number is updated using the cell-face mapping relation [31], providing valuable information about its corresponding cell.

The coupling between the two components of SATES-FDF algorithm is similar as the coupling of LES-FDF in Refs. [50,62–64]. The SATES component offers a solution to the hydrodynamic equations, while the Lagrangian Monte Carlo component calculates the FDF of chemical compositions. The specific-volume transport approach was implemented by solving the specific-volume equation while incorporating a relaxation source term. This source term allowed for the relaxation of the specific-volume FDF towards the SATES specific volume, with a relaxation time step of four times the numerical time step.

### III. VALIDATION IN TECFLAM BURNER

For the simulated TECFLAM burner [39–41], as shown in Fig. 2, the configuration is unrestricted. It consists of an annular slot measuring 15 mm in width, encircling a central bluff body with a diameter of 30 mm. In the experiments conducted for the reactive case, the bluff body was cooled using water to maintain a temperature of 353 K. The generation of swirl was achieved through the manipulation of a movable block geometry. By rotating the block assembly, a theoretical swirl number ranging from 0 to 2 could be attained. The burner was conducted at a swirl number of  $S = 0.75$ . In the reactive case, the fuel–air mixture was fully premixed, possessing an equivalence of  $\phi = 0.83$ . The injection of the mixture was carried out with a volumetric flow rate of  $\dot{Q} = 37.92 \text{ m}^3/\text{h}$ . The Reynolds number was set to  $\text{Re} = 10\,000$ , and the temperature was maintained at 300 K. On the other hand, in the isothermal nonreacting case, air was injected instead of the fuel–air mixture, maintaining the same momentum and temperature. To analyze the velocity fields in both the reacting and nonreacting cases, laser Doppler velocimetry was employed, while the characterization of the flame structure was accomplished through planar laser-induced fluorescence measurements [41]. The mass fractions of  $\text{CO}_2$ ,  $\text{CH}_4$ ,  $\text{N}_2$ ,  $\text{H}_2\text{O}$  and  $\text{O}_2$  were measured using a 1D multiscale Raman-Rayleigh setup. The detailed measurements enable the TECFLAM burner to be

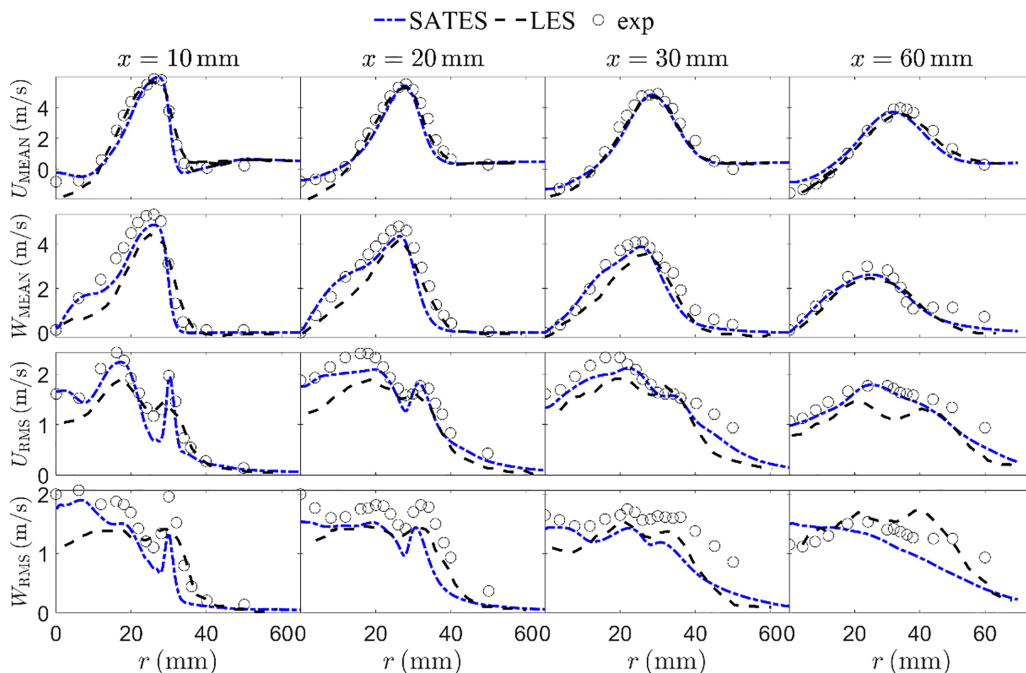


FIG. 3. Radial profiles of the axial ( $U$ )–azimuthal ( $W$ ) mean and rms velocity of the nonreacting case. The profiles are shown at four axial positions ( $x = 10, 20, 30,$  and  $60$  mm). The symbols represent the experimental data [39] and the dotted lines represent the simulated results of SATES (blue) and LES (black) [8].

a benchmark configuration for model validation; for example, DNS was performed to study the isothermal flow [43] and LES combined with the level-set model [43], artificially thickened flame [44], or Eulerian stochastic-field method [8] was performed to study the reacting flow.

In the SATES-FDF simulations, the 25-species methane skeletal mechanism SK25 [65] is employed for oxidation. The bluff-body wall is modeled as a fixed-temperature boundary. In the FDF solver, the heat loss, calculated by a three-layer wall function [66], is taken into account by adjusting the mean sensible enthalpy in the cells adjacent to the bluff-body surface. A similar treatment of boundary conditions can be found in Ref. [67]. The nominal number per cell (npc) is 10; increasing npc to 20 makes no difference to the prediction of mean statistics. The number of grids is  $0.81 \times 10^6$ , with the local refinement in the inner recirculation zone ( $\sim 1\text{-mm}^3$  resolution). The time step is  $4 \times 10^{-5}$  s, where maximum Courant number  $\approx 1.8$ , maximum  $y^+ \approx 10$ . The inlet axial and azimuthal mean-rms velocity is specified according to experimental measurement at  $x = 1$  mm. *In situ* adaptive tabulation [68] has been implemented with the error tolerance being  $2 \times 10^{-4}$  to accelerate chemical reaction integration.

To validate the treatment for turbulence closure using SATES approach, in the isothermal simulation, the mean and rms results of the axial and azimuthal velocities are selected for comparison with the experimental measurements.

Figure 3 illustrates the predicted mean and rms quantities of the axial and azimuthal components of velocity in isothermal nonreacting flow, which are compared to the experimental measurements [39]. Samples have been collected over sufficient amount of time to ensure the convergence of statistics. The predicted and measured axial (azimuthal) components of velocity exhibit a high level of agreement for SATES. The simulated inner (outer) recirculation zone IRZ (ORZ) is also in good agreement with experiment. All the rms velocities also exhibit a reasonable level of agreement with the experiment. Compared with the LES reported in Ref. [8], the level of agreement between simulation and experiment is sufficient for the subsequent analysis.

### A. Flame and flow structures

For the reacting case, simulation was first performed to reach statistically steady state. Then, statistical quantities have been collected over sufficient amount of time to ensure the convergence of statistics. In the analysis, the different flow regimes are identified following the experimental paper [41]. The inner recirculation zone (IRZ) denotes the region where hot products are convected from the reaction zone towards the bluff body. The inner mixing layer (IML) primarily encompasses the flame front. The central annular jet (CAJ) and outer mixing layer (OML) involve the mixing of fuel, downstream hot products, and secondary air. The coflow (CF) corresponds to a zero equivalence ratio [41].

To verify the effectiveness of Eq. (24), the conventional mixing-frequency model  $\Omega_\phi = C_{\phi_{\text{RANS}}} \beta^* \omega$  and  $\Omega_\phi = C_{\phi_{\text{LES}}} \frac{v_r + v}{\Delta^2}$  is also used for comparison, where the former is denoted as RANS-mixing frequency model (RANS-MFM) and the latter is denoted as LES-mixing frequency model (LES-MFM). Equation (24) is denoted as hybrid-mixing frequency model (hybrid-MFM). To ensure the consistency, the parameter  $C_{\phi_{\text{RANS}}}$  and  $C_{\phi_{\text{LES}}}$  should satisfy Eq. (25). The value of  $C_{\phi_{\text{RANS}}}$  and  $C_{\text{VLES}}$  is determined based on a sensitivity study by matching the computed statistics with the experimental data, which essentially yields  $C_{\text{VLES}} = 0.61$  and  $C_{\phi_{\text{RANS}}} \approx 30$ . In this study, the IEM mixing model is employed for demonstration. Similar results are obtained with MC and EMST (not shown).

To provide an overall qualitative representation of the flame structure, time-averaged and transient of temperature, species, equivalence ratio, velocity, fraction of modeled TKE, and mixing frequency simulated by SATES-FDF with hybrid-MFM are shown in Fig. 4. In the experiment, the flame exhibits a weak M-shaped pattern which is also observed in simulation. However, the flame on the two wings locates further downstream in the simulation, which indicates the underestimated heat-release rate. Increasing  $C_{\phi_{\text{RANS}}}$  will subsequently lead to the stabilization of the flame closer to the blunt wall. Due to the heat loss, the temperature around the bluff body is lower than 2040 K, which is the adiabatic flame temperature for this mixture [39]. An isosurface of OH concentration represents the flame front, primarily situated within the IML. The equivalence ratio remains relatively constant near the bluff body. However, as we move downstream, the main flow mixes with secondary air near the reaction zone, leading to a decrease in the equivalence ratio. Figures 4(e) and 4(f) are shown to illustrate the differences in mixing-frequency predictions among different mixing-frequency models. Specifically, the hybrid-MFM model was employed in the simulation, complemented by calculations from two additional models for comparative analysis. By analyzing the distribution of  $f_r$  ( $f_r = F_r^{0.5}$ ), it can be observed that the RANS mode ( $f_r = 1$ ) is mainly near the wall, while the LES mode ( $0 < f_r < 1$ ) is predominantly in the region far from the wall. Further observation on the distribution of  $f_r$  and  $\Omega_{\phi_{\text{hybrid}}} - \Omega_{\phi_{\text{LES}}}$  uncovers discrepancies in mixing-frequency predictions at  $f_r = 1$ , indicating the RANS mode. Notably, compared with hybrid-MFM, LES-MFM forecasts a lower mixing frequency near the wall, in contrast to RANS-MFM, which predicts a lower mixing frequency at regions away from the wall.

It is worth appreciating that SATES is like LES, which approaches DNS as computational grids get refined. Consequently, unlike RANS, SATES only reaches grid convergence at the DNS limit; this greatly diminishes the value of checking its grid convergence. Instead, the study on grid sensitivity of SATES has been performed in Refs. [23,24,27,28], in which SATES has demonstrated the similar accuracy as LES using a much finer grid, illustrating the advantages of SATES. Despite that the grid-convergence test was not performed in this study, grid resolution can be verified through the distribution of  $f_r$  shown in Fig. 4(e). Observations from the figure below indicate that in regions like shear layers and recirculation cores, the LES mode dominates, effectively capturing complex phenomena like separated flows, shear layers, and vortex breakup. This suggests that the grid resolution is sufficient to meet requirement for SATES-FDF simulation of the TECFLAM case.

For comparison, Figs. 5 and 6 illustrate the time-averaged axial velocity, equivalence ratio, temperature, and OH mass fraction, simulated by SATES-FDF using the RANS-MFM and LES-MFM, respectively. Compared with Fig 4, the results obtained by RANS-MFM and LES-MFM exhibit

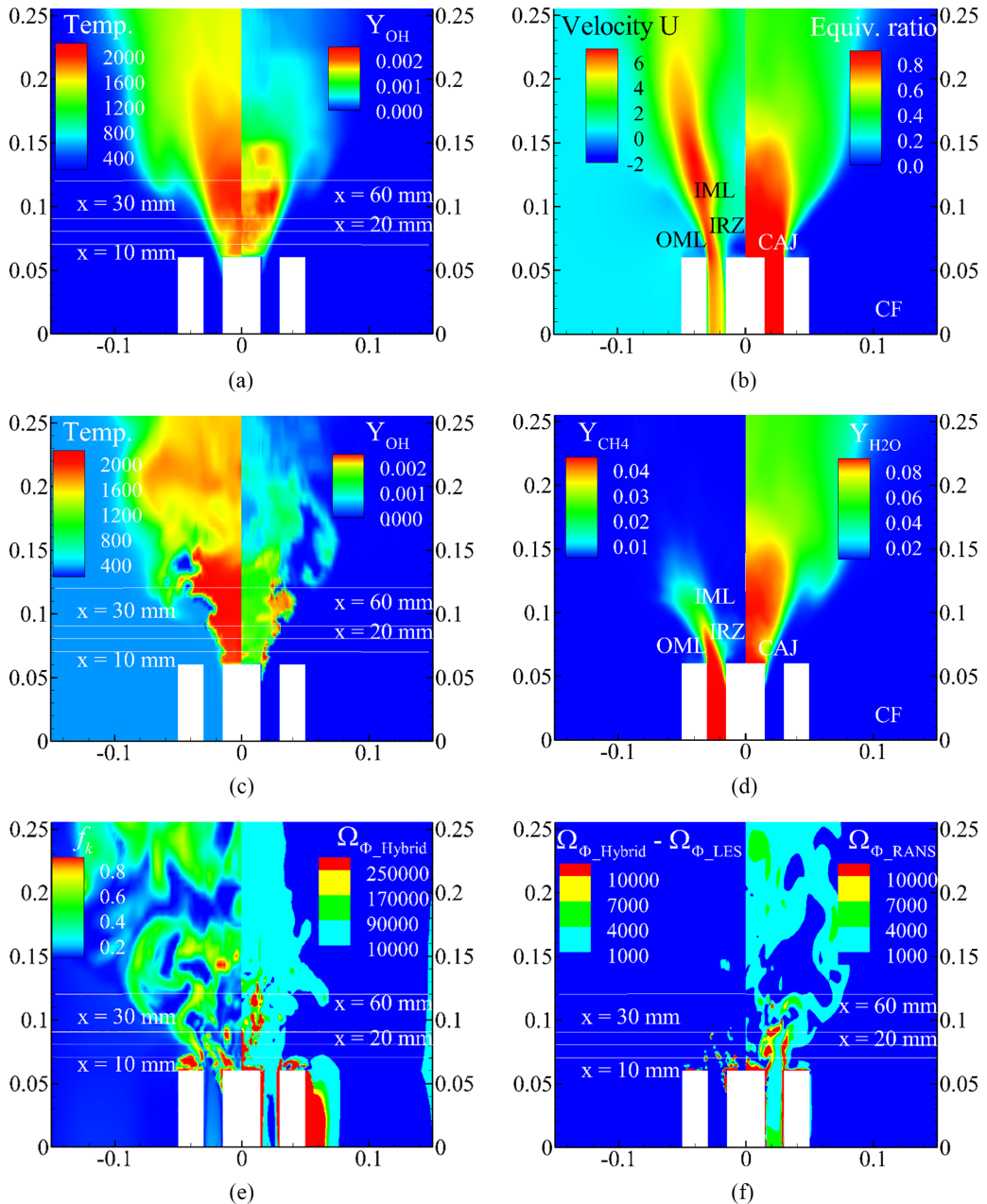


FIG. 4. The reacting case simulated by SATE-FDF with hybrid-MFM. (a) Time-averaged temperature and mass fraction of OH. (b) Time-averaged axial velocity, equivalence ratio (c); snapshots of temperature and mass fraction of OH (d) time-averaged mass fraction of CH<sub>4</sub> and H<sub>2</sub>O. (e) The fraction of the modeled turbulent kinetic energy in the total turbulent kinetic energy and mixing frequency predicted by hybrid-MFM. (f) The mixing frequency predicted by hybrid-MFM minus mixing frequency predicted by LES-MFM and mixing frequency predicted by RANS-MFM (IRZ, inner recirculation zone; IML, inner mixing layer; CAJ, central annular jet; OML, outer mixing layer; CF, coflow).

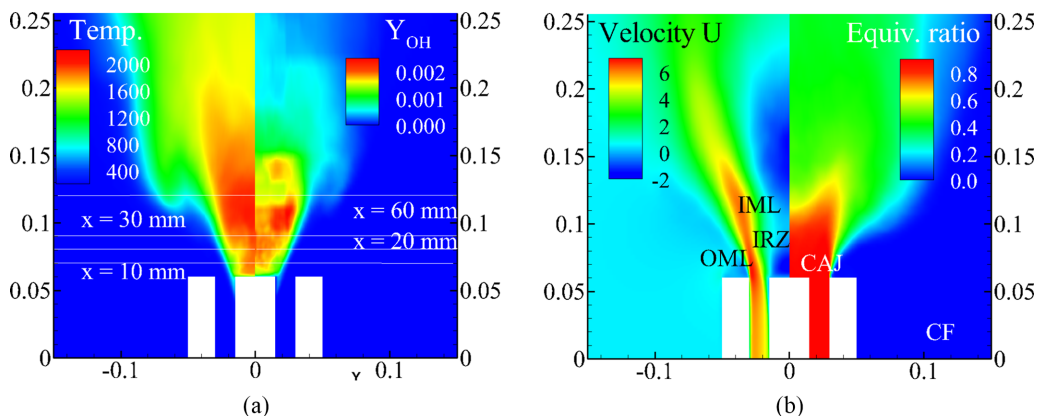


FIG. 5. The reacting case simulated by SATE-FDF with RANS-MFM. (a) Time-averaged temperature and mass fraction of OH. (b) Time-averaged axial velocity, equivalence ratio.

reduced velocity expansions, leading to the formation of larger recirculation regions and allowing air to be entrained into the premixed region. Consequently, the equivalence ratio in the recirculation region decreases, affecting the flame structure.

### B. Velocity and composition profiles

The means and rms of the axial and azimuthal velocities with different mixing-frequency models simulated by SATES-FDF are shown in Fig. 7, respectively. It is observed that the results of these three different mixing-frequency models are quite different. Focusing on the mean velocities, the mixing-frequency model hybrid-MFM has a better overall agreement with experimental data compared to RANS-MFM or LES-MFM. All the rms velocities are qualitatively consistent with the experiment, and are insensitive to different mixing-frequency models. One obvious disagreement between simulation and experiment is the mean azimuthal velocity when using LES-MFM. The variations in velocity expansion may be attributed to the significant influence of three different mixing-frequency models on the predicted mixing frequency, which in turn affects the finite reaction rates and the heat-release rate.

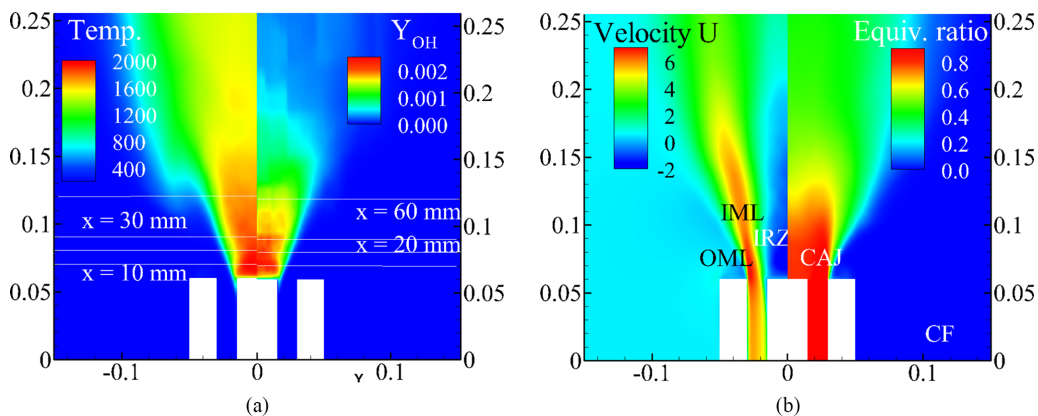


FIG. 6. The reacting case simulated by SATE-FDF with LES-MFM. (a) Time-averaged temperature and mass fraction of OH. (b) Time-averaged axial velocity, equivalence ratio.

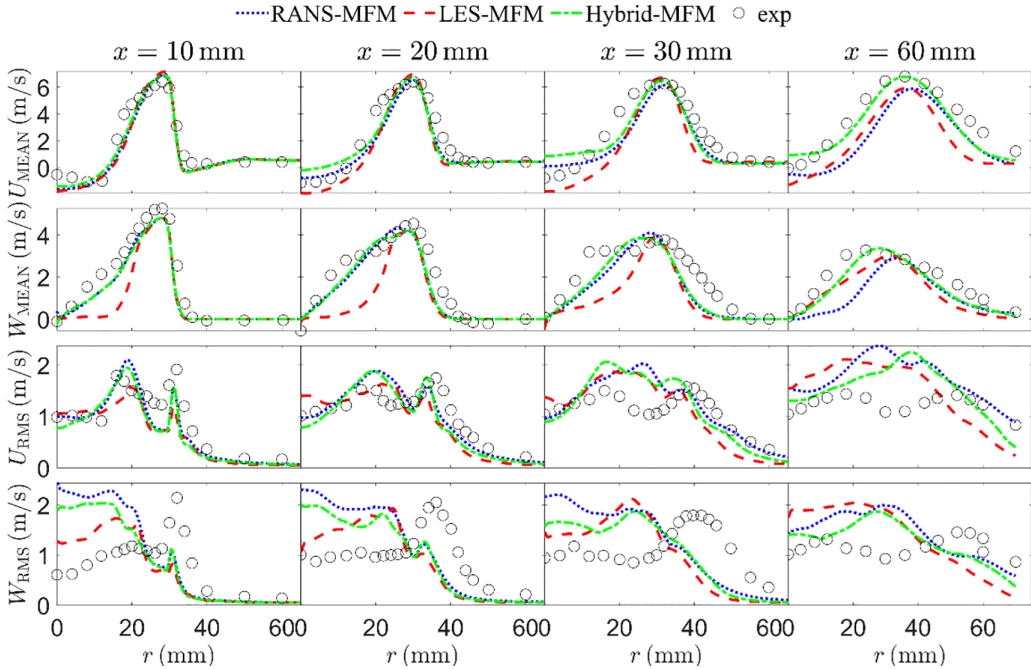


FIG. 7. Radial profiles of the axial ( $U$ )–azimuthal ( $W$ ) mean and rms velocity of the reacting case simulated by SATES-FDF. The profiles are shown at four axial positions ( $x = 10, 20, 30,$  and  $60$  mm). The symbols represent the experimental data [39] and the lines of different color represent the simulation results with different methods.

The means and rms of the temperature, equivalence with different mixing-frequency models simulated by SATES-FDF, are shown in Fig. 8, respectively. It is observed that the results of these three different mixing-frequency models are quite different. The mean temperature in experiment first increases and then decreases along the radial direction ( $r = 0 - 30$  mm) at the inner recirculation zone, which is not captured by the simulation. The uncertainty in the experimental conditions at the bluff-body wall may be the reason, and the fixed temperature condition used in the simulation might not be adequate to represent the nonuniform wall temperature caused by water cooling. The excessive and unsteady heat exchange may lead to less flame expansion and eventually result in lower overall predicted mean temperature and higher predicted rms temperature around the bluff body compared with experiment. In addition, the mean-rms temperature of experiment gets a second peak around  $r = 40$  mm,  $x = 20-30$  mm, which is delayed to  $r = 60$  mm,  $x = 60$  mm in the simulation due to less flame expansion. Among the three mixing-frequency models, only hybrid-MFM captures the second peak.

As shown in Fig. 8, the experimental equivalence [39] is almost a constant 0.833 around  $r = 0-30$  mm at the inner recirculation zone, and then drops down to around  $r = 30-60$  mm outside the inner recirculation zone. Compared by simulated equivalence, hybrid-MFM has a better overall agreement with experiments than RANS-MFM and LES-MFM, where LES-MFM does not form a premixed combustion flame in the all-inner circulation zone and RANS-MFM has a narrower premix combustion region than the experiment. The worse performance of RANS-MFM and LES-MFM may be due to mixing of air which comes from vortex core breaking in advance caused by the low heat release. The higher experimental rms equivalence than simulation at the inner recirculation zone may be due to the transients at the inlet [41], which is not considered in the simulation. Thus, in general, the correct prediction of the expansion effect caused by temperature increase is a

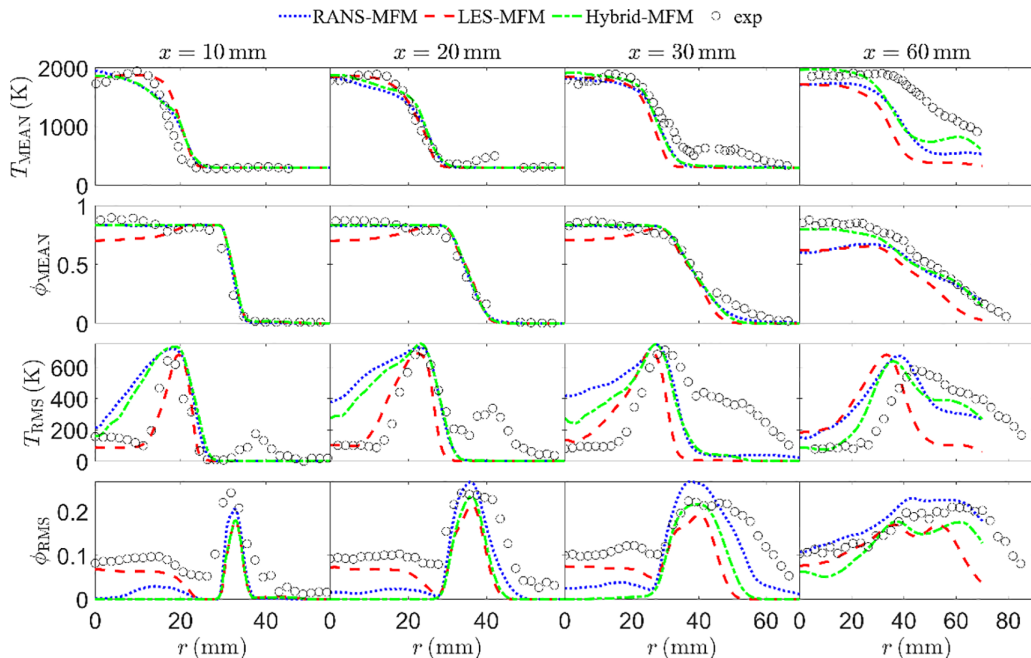


FIG. 8. Radial profiles of the mean and rms temperature ( $T$ )–equivalence ( $\phi$ ) of the reacting case simulated by SATES-FDF. The profiles are shown at four axial positions ( $x = 10, 20, 30,$  and  $60$  mm). The symbols represent the experimental data [39] and the lines of different colors represent the simulation results with different methods.

crucial factor for the swirl field, which is captured by hybrid-MFM, but not by RANS-MFM and LES-MFM.

The means and rms of the mass fraction of  $\text{CH}_4$ ,  $\text{CO}_2$ , and  $\text{O}_2$  with different mixing-frequency models simulated by SATES-FDF are shown in Fig. 9, respectively. The simulated results of  $\text{CH}_4$  exhibit a good level of agreement with experimental measurements. In the inner circulation zone,  $\text{CH}_4$  is consumed, then increases at IML and CAJ, and finally decreases to zero at OML and CF along the radial direction, which is reasonably captured by simulation. The mass fraction of  $\text{CH}_4$  is in reasonable agreement with experiments around  $r = 0 - 30$  mm, but is overpredicted for  $r > 30$  mm, which is probably due to the underestimated flame expansion observed in the velocity and temperature results in Fig. 7 and Fig. 8. The mass fractions of  $\text{CO}_2$  and  $\text{O}_2$  also exhibit similar trends as temperature. The performance of three mixing-frequency models in predicting mass fractions of  $\text{CH}_4$ ,  $\text{O}_2$ , and  $\text{CO}_2$  is very similar.

### C. Scatter plots and conditional statistics

Since the SATES-FDF simulation with hybrid-MFM demonstrates satisfactory agreement with the experimental data concerning the mean flow and flame statistics, we can now focus on examining the instantaneous thermochemical state. This is particularly intriguing because the SATES-FDF simulation provides detailed three-dimensional information about the flame at any given moment. The instantaneous particle information is obtained by selecting five time instances with an equal time spacing from the fully developed and statistical steady flame. Note that only 1/5 of these particles have been presented in the following figures.

Figure 10 illustrates scatter plots of temperature-conditioned position at various axial planes. In these plots, the temperature of Lagrangian particles is plotted against their radial position. Both the

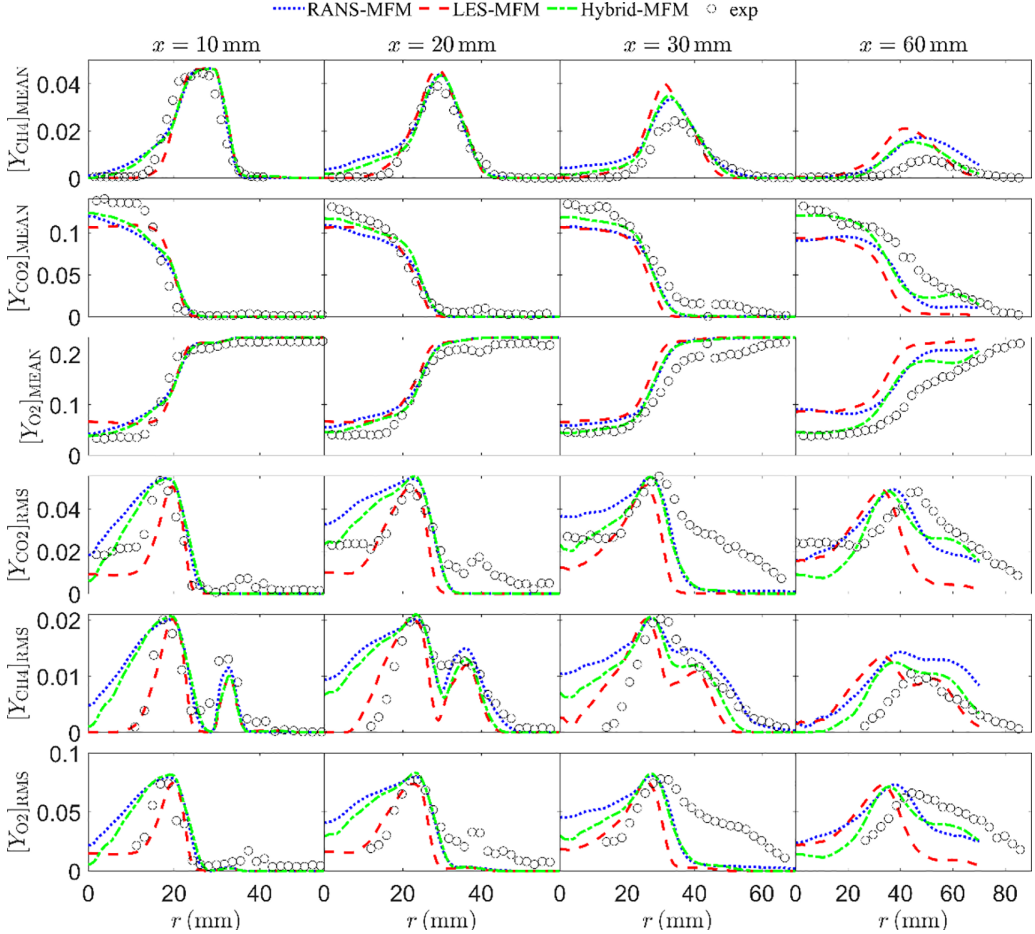


FIG. 9. Radial profiles of the mean and rms mass fraction of  $\text{CH}_4$ ,  $\text{CO}_2$ , and  $\text{O}_2$  ( $Y_{\text{CH}_4}$ ,  $Y_{\text{CO}_2}$ , and  $Y_{\text{O}_2}$ ) of the reacting case simulated by SATES-FDF. The profiles are shown at four axial positions ( $x = 10, 20, 30$ , and  $60$  mm). The symbols represent the experimental data [39] and the lines of different colors represent the simulation results with different methods.

experimental results and simulations exhibit a bimodal pattern, where intermediate temperatures increase as the flame brush thickness grows, further downstream from the swirler exit. Among the three mixing-frequency models, only hybrid-MFM captures this most accurately.

Figures 11 and 12 show the PDFs of temperature and molar concentration of  $\text{H}_2\text{O}$ , respectively, measured at  $x = 30$  mm. These measurements were conducted for three distinct ranges of equivalence ratios ( $\phi < 0.65$ ,  $0.65 < \phi < 0.75$ , and  $\phi > 0.75$ ). For comparison purposes, the experimental single-shot PDFs are also incorporated in the figures.

The first zone ( $\phi < 0.65$ ) primarily encompasses the CF region, as well as the region where some products and unburned gas are transported to CF region due to the influence of the outer recirculation zone. This region is characterized by low temperatures and few products. As shown in Fig. 11 and Fig. 12, the simulation results obtained by hybrid-MFM demonstrate better overall agreement with the experiment compared to the results obtained by RANS-MFM and can capture the main characteristics of this region. On the other hand, the simulation obtained by RANS-MFM predicts a high probability near  $T = 1700$  K, which may be attributed to excessive mixing with coflow secondary air.

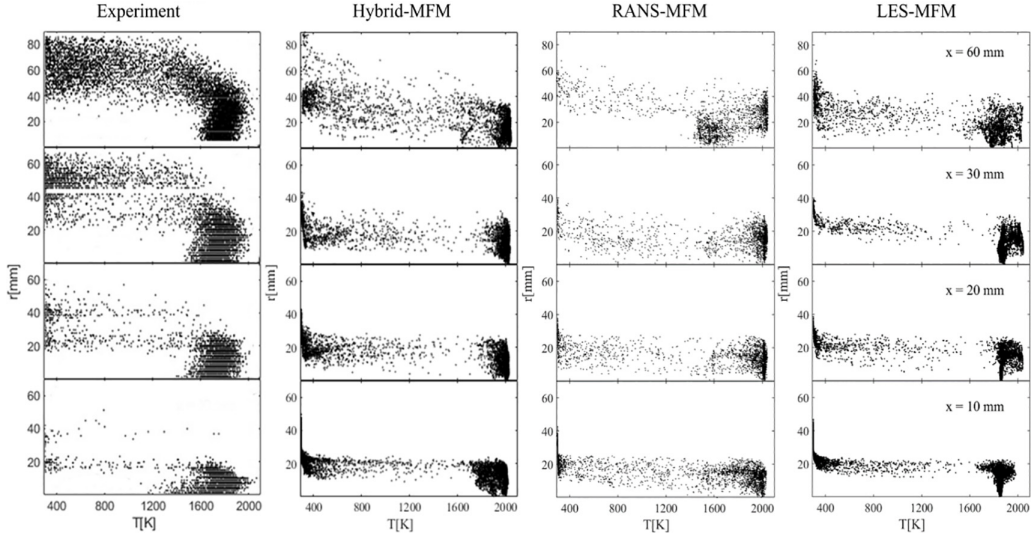


FIG. 10. Single-shot scatter plots of radial position conditioned on temperature for four different  $x$  planes ( $x = 10, 20, 30,$  and  $60$  mm). A comparison of the experiment [39] and the simulation with SATES-FDF is shown.

The second zone ( $0.65 < \phi < 0.75$ ) primarily encompasses the partial IML region, partial CAJ region, and partial OML region, which is a very narrow region, closing to nozzle and the fuel mixing with the air coming from the same direction. At  $x = 30$  mm, the flame front exhibits wrinkling and penetration within this region. Consequently, the experimental results indicate a bimodal distribution in PDFs of temperature and the mole fraction of  $H_2O$ . The overall agreement between the simulation results obtained by hybrid-MFM and the experiments surpasses that of RANS-MFM and LES-MFM. This disparity arises from the ability to reproduce bimodal behavior in both the hybrid-MFM simulation and the experimental results, which is not observed in the LES-MFM simulation. In the RANS-MFM simulation, the peak in the low-temperature region

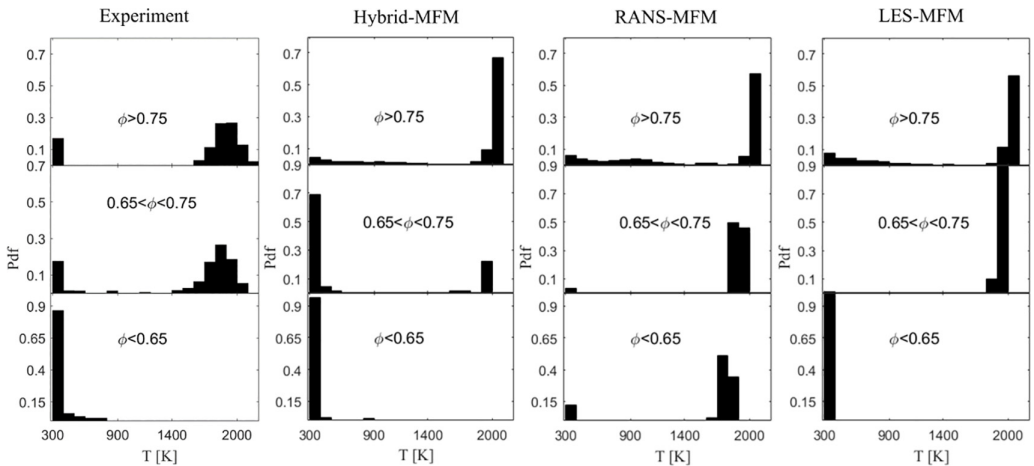


FIG. 11. PDFs of temperature for three different ranges of equivalence ratios at  $x = 30$  mm. A comparison of the experiment [39] and the simulation with SATES-FDF is shown.

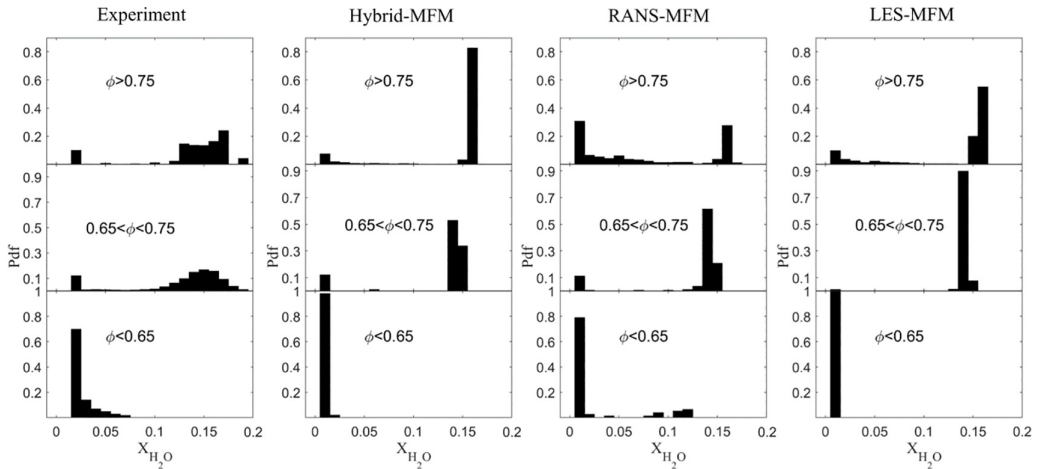


FIG. 12. PDFs of mole fraction of  $\text{H}_2\text{O}$  for three different ranges of equivalence ratios at  $x = 30$  mm. A comparison of the experiment [39] and the simulation with SATES-FDF is shown.

is reduced. This is primarily attributed to the fact that air mixing reduces the equivalence in the reaction zone, causing combustion to transpire in regions with lower equivalence, thereby leading to unimodal behavior in the products and temperature.

The third zone ( $\phi > 0.75$ ) contains the entire IRZ region along with CAJ region and parts of the IML region. Here, the dilution with secondary air is minimal. The PDFs in Figs. 11 and 12 exhibit a bimodal distribution, representing undiluted fuel and fully burnt gas, in both the experiment and simulation. However, the maximum temperatures predicted by the three different mixing-frequency models are consistently higher than those observed in the experiment. During the experiment, the temperature distribution is centered around 1800 K. However, the simulation results reveal a clustering of temperatures around the adiabatic temperature of 2040 K, suggesting a higher probability of reaching a chemical equilibrium state. This inconsistency could be attributed to the previously mentioned wall condition of the bluff body, which leads to inadequate prediction of intermittent heat losses in the inner recirculation zone. The simulation results obtained by RANS-MFM indicate a high probability at a low molar fraction of  $\text{H}_2\text{O}$ , which may be attributed to increased air mixing in the inner recirculation zone. Consequently, the reaction occurs at the low equivalence, resulting in a larger amount of undiluted fuel remaining at the high equivalence.

Further analysis of the described observations can be conducted by examining scatter plots depicting the equivalence,  $\text{CH}_4$  and  $\text{H}_2\text{O}$  in relation to temperature. These scatter plots illustrate the data for two distinct axial positions, namely  $x = 10$  mm and  $x = 30$  mm in Figs. 13 and 14, respectively. At  $x = 10$  mm, the particles sampled from the IRZ in the experiment are predominantly concentrated in the high-temperature region, characterized by a very low  $\text{CH}_4$  fraction, high  $\text{H}_2\text{O}$  content, and an equivalence ratio of approximately 0.83 in a state of chemical equilibrium. The particles sampled from ISL and CAJ show a similar concentration around an equivalence ratio of 0.83. The particles sampled from OSL are concentrated in the low-temperature region, while particles sampled from CF are concentrated in both the low equivalence ratio and low-temperature region. Among the three models mentioned, the RANS-MFM simulation results show significant deviations from the experimental data. Conversely, the other two models exhibit closer agreement with the experimental results. At  $x = 30$  mm, the experimental results demonstrate similar trends to those observed at  $x = 10$  mm. However, there is a higher level of scattering in the data, which the simulation fails to reproduce. This discrepancy may be attributed to a lack of statistical particle number, as there is a limited number of particles in the OML and CF regions. Nevertheless,

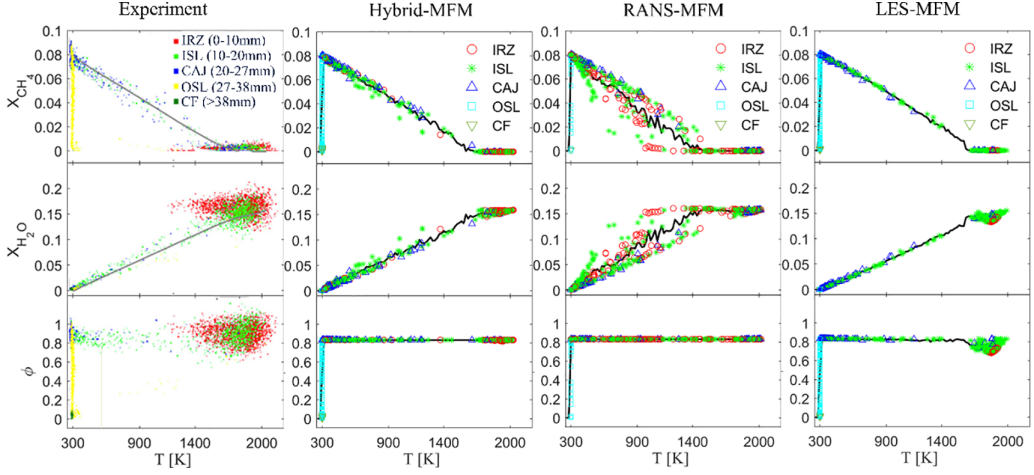


FIG. 13. Simulated scatter plots of equivalence ratio and mole fractions of  $\text{CH}_4$  and  $\text{H}_2\text{O}$  vs temperature at  $x = 10$  mm. The black (gray) line is the mean value. A comparison of the experiment [39] and the simulation with SATES-FDF is shown.

the RANS-MFM simulation results still display significant inconsistency with the experimental findings.

#### IV. CONCLUSION

Transported FDF in hybrid RANS-LES method was investigated theoretically, including the basic definition, mixing model, and scalar-mixing rate model. The main conclusions follow:

(1) Due to the inconsistency of scalar-mixing rate model between RANS mode and LES mode in hybrid RANS-LES method, four modeling criteria are proposed via dimensional analysis to ensure the consistency for the sake of realizability. The original scalar-mixing rate model in RANS framework ( $\Omega_\phi = C_{\phi_{\text{RANS}}} \beta^* \omega$ ) or LES framework ( $\Omega_\phi = C_{\phi_{\text{LES}}} \frac{v_i + v_j}{\Delta^2}$ ) was proved to violate these

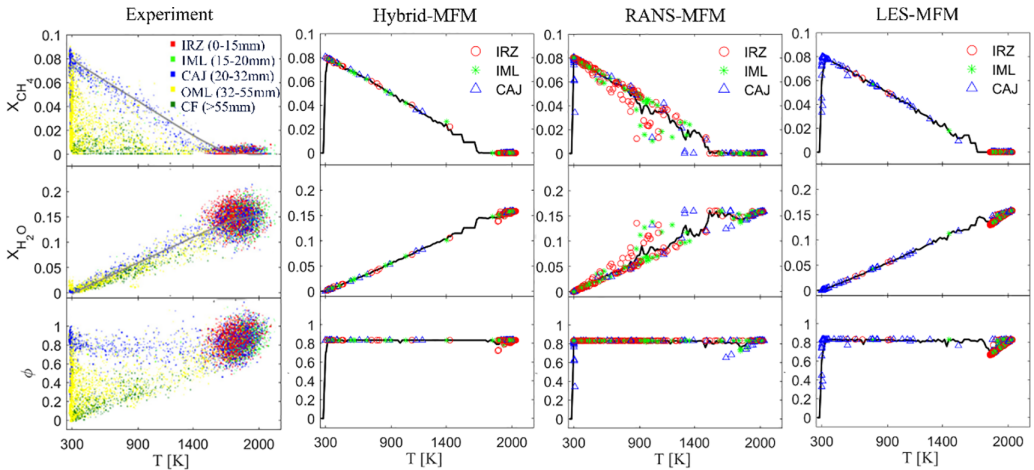


FIG. 14. Simulated scatter plots of equivalence ratio and mole fractions of  $\text{CH}_4$  and  $\text{H}_2\text{O}$  vs temperature at  $x = 30$  mm. The black (gray) line is the mean value. A comparison of the experiment [39] and the simulation with SATES-FDF is shown.

criteria. Then, a scalar-mixing rate model was proposed by dimensional analysis with a length scale  $L_{\text{hybrid}}$ , which is obtained by taking the minimum value of turbulent cutoff length scale and integral length scale. The proposed SATES-FDF can be extended to several more hybrid RANS-LES methods due to H equivalence.

(2) To establish a correlation between  $C_{\phi_{\text{RANS}}}$  and  $C_{\phi_{\text{LES}}}$  in the scalar-mixing rate model, the adopted RANS model is assumed to be identical to the standard Smagorinsky-Wall-Adapting Local Eddy (WALE) LES model when  $F_r = 1$ . Alternatively, for a specific hybrid RANS-LES strategy, the trigger between RANS mode and LES mode naturally provides a bridge between  $C_{\phi_{\text{RANS}}}$  and  $C_{\phi_{\text{LES}}}$ .

With SATES based on  $k-\omega$  SST model, the SATES-FDF approach is demonstrated in the standard turbulent premixed swirling burner TECFLAM. Results show that for the isothermal case, good agreement with the experimental flow data is achieved with SATES-FDF on a coarse grid of  $0.81 \times 10^6$  cells, which is comparable to reported LES and quasi-DNS simulations on much finer resolution. For the reacting case, the proposed mixing-frequency model hybrid-MFM ( $\Omega_\phi = C_{\phi_{\text{hybrid}}} \frac{u_i + u_j}{L_{\text{hybrid}}^2}$ ) has a better overall agreement with experiments than the classic mixing-frequency model RANS-MFM ( $\Omega_\phi = C_{\phi_{\text{RANS}}} \beta^* \omega$ ) and LES-MFM ( $\Omega_\phi = C_{\phi_{\text{LES}}} \frac{u_i + u_j}{\Delta^2}$ ) in terms of the mean velocity field, the mean temperature, and the mean equivalence. The poorer performance of RANS-MFM and LES-MFM might be attributed to their underprediction of the heat-release rate. This further causes an underestimated velocity expansion and alters the structure of the recirculation zone. Consequently, fuel mixes with more secondary air from the coflow within the recirculation zone, thus impacting the flame structure. The mass fractions of  $\text{CH}_4$ ,  $\text{CO}_2$ , and  $\text{O}_2$  also show consistent trends with the temperature. The observed behavior in the experiments was found to be consistent with the instantaneous scatter plots and conditional PDFs of the temperature, exhibiting a comparable bimodal behavior.

#### ACKNOWLEDGMENTS

This work was supported by the National Natural Science Foundation of China (Grants No. 52025062 and No. 52106166). The authors also acknowledge High-Performance Computing Centre in Tsinghua University for providing computational resource.

#### APPENDIX: TRANSPORTED FDF IN GENERAL HYBRID RANS-LES METHOD

Considering the different existing hybrid RANS-LES methods, a unified framework is explored to extend SATES-FDF to general hybrid RANS-LES method. As suggested by Pope [45], turbulent resolution could be measured by the fraction of the modeled turbulent kinetic energy in the total turbulent kinetic energy,  $f_k$ , similar to  $f_r$  in SATES, which could then be employed to classify the local turbulence modes, e.g., DNS mode if  $f_k \rightarrow 0$ , LES mode if  $f_k$  is between 0 and 0.2, VLES mode if  $f_k$  is between 0.2 and 1, and RANS mode if  $f_k \rightarrow 1$ . One can formulate a unified framework for FDF in general hybrid RANS-LES method with H equivalence [69,70], in which different hybrid RANS-LES methods are formulated with the same closure in governing equations, and the same energy partition  $f_k$  is employed for mode transition.

##### 1. H equivalence of hybrid RANS-LES method

The H equivalence by Davidson and Freiss [69] and Freiss and co-workers [70] evaluates the equivalence of hybrid RANS-LES method and allows various hybrid methods to be regarded as models for the same system of equations. For example, a DES-like model (DES [18]) has been demonstrated to be H equivalent with the PANS-like model [71] under stationary, inhomogeneous conditions. In this section, the H equivalence among SATES [23,24] (VLES-like), classic DES [18] (DES-like), and PANS [19–21] (PANS-like) models is demonstrated by analyzing the base RANS standard  $k-\varepsilon$  model and the demonstration is also applicable to the base RANS  $k-\omega$  SST model.

Define the subfilter turbulent kinetic energy as  $k_m$ , the total turbulent kinetic energy as  $k_{\text{tot}}$ , subfilter dissipation rate as  $\varepsilon_m$ , and the total dissipation rate as  $\varepsilon_{\text{tot}}$ , which satisfy  $\nu_t = \frac{1}{\beta^*} \frac{k_m^2}{\varepsilon_m}$  [72]. Assume this satisfies self-consistency, i.e.,  $\varepsilon_m = \varepsilon$ . For SATES,  $\nu_t = \frac{1}{\beta^*} \frac{k_m^2}{\varepsilon_m} = F_r \cdot \frac{1}{\beta^*} \frac{k^2}{\varepsilon}$ , thus  $k = \frac{k_m}{\sqrt{F_r}}$ . For classic DES-like and PANS-like models, the variable of governing equations is naturally  $k_m$  and  $\varepsilon_m$ . Therefore, considering  $F_r$  as a constant for convenience, which is similar to the constant parameter  $f_k$  in PANS's demonstration, the governing equations can be rewritten into

$$\frac{\partial \rho k_m}{\partial t} + \frac{\partial \rho \bar{u}_j k_m}{\partial x_j} = \rho P_{k1} - \psi \rho \varepsilon_m + \rho D_k, \quad (\text{A1})$$

$$\frac{\partial \rho \varepsilon_m}{\partial t} + \frac{\partial \rho \bar{u}_j \varepsilon_m}{\partial x_j} = \frac{\varepsilon_m}{k_m} (C_{\varepsilon 1} \rho P_{k1} - C_{\varepsilon 2}^* \rho \varepsilon_m) + \rho D_\varepsilon, \quad (\text{A2})$$

where  $P_{k1} = \sqrt{F_r} P_k$ ,  $\psi = \sqrt{F_r}$ ,  $C_{\varepsilon 2}^* = \sqrt{F_r} C_{\varepsilon 2}$  in SATES,  $P_{k1} = P_k$ ,  $\psi = F_{\text{DES}} = \max(\frac{L_c}{L_c}, 1)$ ,  $C_{\varepsilon 2}^* = C_{\varepsilon 2}$  in DES, and  $P_{k1} = P_k$ ,  $\psi = 1$ ,  $C_{\varepsilon 2}^* = C_{\varepsilon 1} + \frac{f_k}{f_\varepsilon} (C_{\varepsilon 2} - C_{\varepsilon 1})$  in PANS, usually  $f_\varepsilon = 1.0$  [19],  $D_k = \frac{1}{\rho} \frac{\partial}{\partial x_j} [(\mu + \frac{\mu_t}{\sigma_k}) \frac{\partial k_m}{\partial x_j}]$  and  $D_\varepsilon = \frac{1}{\rho} \frac{\partial}{\partial x_j} [(\mu + \frac{\mu_t}{\sigma_\varepsilon}) \frac{\partial \varepsilon_m}{\partial x_j}]$ .

In the following, the H equivalence among three hybrid RANS-LES methods under equilibrium layers will be first proved, and then stationary, inhomogeneous conditions will be considered.

In equilibrium layers, the turbulent timescale  $\tau_m = \frac{k_m}{\varepsilon_m}$  asymptotically tends to equilibrium, i.e.,  $\frac{D\tau_m}{Dt} = 0$ , and  $D_k$  and  $D_\varepsilon$  can be ignorable. Thus, we can get

$$\gamma_1 (C_{\varepsilon 1} - 1) |S| k_m = (C_{\varepsilon 2}^* - \psi) \varepsilon, \quad (\text{A3})$$

where  $\gamma_1 = \frac{P_{k1}}{S k_m}$ ,  $|S| = \sqrt{2 \tilde{S}_{ij} \tilde{S}_{ij}}$ .

Differentiation of Eq. (A3), by considering infinitesimal perturbations  $\delta\gamma_1$ ,  $\delta|S|$ ,  $\delta k_m$ ,  $\delta C_{\varepsilon 2}^*$ , and  $\delta\psi$  of the variables, yields

$$\frac{\delta\gamma_1}{\gamma_1} + \frac{\delta|S|}{|S|} + \frac{\delta k_m}{k_m} = \frac{\delta C_{\varepsilon 2}^* - \delta\psi}{C_{\varepsilon 2}^* - \psi}. \quad (\text{A4})$$

Let  $\gamma_2 = \frac{P_\varepsilon}{S k_m}$ ; the left-hand side is the same in SATES, DES, and PANS, i.e.,  $\frac{\delta\gamma_2}{\gamma_2} + \frac{\delta|S|}{|S|} + \frac{\delta k_m}{k_m}$ . Integrating the right-hand side from RANS ( $\psi = 1$ ,  $C_{\varepsilon 2}^* = C_{\varepsilon 2}$ ) to LES conditions ( $\psi$ ,  $C_{\varepsilon 2}^*$ ),

$$\begin{aligned} \int_{C_{\varepsilon 2,1}}^{C_{\varepsilon 2}^*, \psi} \frac{\delta C_{\varepsilon 2}^* - \delta\psi}{C_{\varepsilon 2}^* - \psi} &= \ln \left( \frac{C_{\varepsilon 2}^* - \psi}{C_{\varepsilon 2} - 1} \right) = \ln(\sqrt{F_r}) \\ &= \ln \left( \frac{C_{\varepsilon 1} + \frac{f_k}{f_\varepsilon} (C_{\varepsilon 2} - C_{\varepsilon 1}) - 1}{C_{\varepsilon 2} - 1} \right) = \ln \left( \frac{C_{\varepsilon 2} - F_{\text{DES}}}{C_{\varepsilon 2} - 1} \right). \end{aligned} \quad (\text{A5})$$

Therefore,

$$f_k = \frac{\sqrt{F_r} (C_{\varepsilon 2} - 1) - (C_{\varepsilon 1} - 1)}{C_{\varepsilon 2} - C_{\varepsilon 1}} = 1 - \frac{F_{\text{DES}} - 1}{C_{\varepsilon 2} - C_{\varepsilon 1}}. \quad (\text{A6})$$

To ensure a tractable system of equations, the analysis reintroduces the modeled diffusion and transport effects into Eqs. (A4) and (A5) with additional restrictions. In this context, it is assumed that both  $k_m$  and  $\varepsilon_m$  are in equilibrium along mean streamlines. The system of equations can then be written as follows:

$$P_{k1} - \psi \varepsilon_m + D_k = 0, \quad (\text{A7})$$

$$\frac{\varepsilon_m}{k_m} (C_{\varepsilon 1} P_{k1} - C_{\varepsilon 2}^* \varepsilon_m) + D_\varepsilon = 0. \quad (\text{A8})$$

Assuming self-consistency ( $\delta\varepsilon_m = 0$ ), the resulting equation for the infinitesimal perturbations is

$$\delta P_{k1} - \varepsilon_m \delta\psi + \delta D_k = 0, \quad (\text{A9})$$

$$C_{\varepsilon 1} \frac{\varepsilon_m}{k_m} P_{k1} \left( \frac{\delta P_{k1}}{P_{k1}} - \frac{\delta k_m}{k_m} \right) - C_{\varepsilon 2}^* \frac{\varepsilon_m^2}{k_m} \left( \frac{\delta C_{\varepsilon 2}^*}{C_{\varepsilon 2}^*} - \frac{\delta k_m}{k_m} \right) + \delta D_\varepsilon = 0. \quad (\text{A10})$$

Ignoring the laminar viscosity,

$$\frac{\delta D_k}{D_k} = 3 \frac{\delta k_m}{k_m}, \quad (\text{A11})$$

$$\frac{\delta D_\varepsilon}{D_\varepsilon} = 2 \frac{\delta k_m}{k_m}. \quad (\text{A12})$$

Combining the above Eqs. (A7)–(A12),

$$\frac{\delta C_{\varepsilon 2}^* - C_{\varepsilon 1} \delta\psi}{C_{\varepsilon 2}^* - \psi C_{\varepsilon 1}} = 3 \frac{\delta k_m}{k_m}. \quad (\text{A13})$$

Integrating from RANS ( $\psi = 1$ ,  $C_{\varepsilon 2}^* = C_{\varepsilon 2}$ ) to LES conditions ( $\psi$ ,  $C_{\varepsilon 2}^*$ ),

$$\begin{aligned} \int_{C_{\varepsilon 2}, 1}^{C_{\varepsilon 2}^*, \psi} \frac{\delta C_{\varepsilon 2}^* - C_{\varepsilon 1} \delta\psi}{C_{\varepsilon 2}^* - \psi C_{\varepsilon 1}} &= \ln \frac{C_{\varepsilon 2}^* - \psi C_{\varepsilon 1}}{C_{\varepsilon 2} - C_{\varepsilon 1}} = (\text{VLES}) \ln \sqrt{F_r} = (\text{PANS}) \ln f_k \\ &= (\text{DES}) \ln \frac{C_{\varepsilon 2} - F_{\text{DES}} C_{\varepsilon 1}}{C_{\varepsilon 2} - C_{\varepsilon 1}}. \end{aligned} \quad (\text{A14})$$

Therefore,

$$f_k = \sqrt{F_r} = \frac{C_{\varepsilon 2} - F_{\text{DES}} C_{\varepsilon 1}}{C_{\varepsilon 2} - C_{\varepsilon 1}}. \quad (\text{A15})$$

It is worth mentioning that  $f_k = \sqrt{F_r} = f_r$ , where  $f_k$  and  $f_r$  are both defined as the ratio of unresolved TKE to total TKE, but the modeling for  $f_k$  and  $f_r$  may be quite different. This reveals the differences and similarities of different hybrid RANS-LES methods.

## 2. FDF coupled with general hybrid RANS-LES method

The interpretation and implementation of FDF in SATES can be directly extended to the above hybrid RANS-LES method methods, except that the potential inconsistency in scalar-mixing rate model should be properly addressed. With Eq. (A15) proved by H equivalence, one could unify different resolution control functions, e.g.,  $F_r$  in VLES-like models,  $F_{\text{DES}}$  in DES-like models, and  $f_k$  in PANS-like models, such that a common resolution control function could represent different hybrid RANS-LES methods. For example, if  $f_k$  is chosen as the common resolution control function, the modeling criteria of scalar-mixing rate could be modified as follows:

- (1) In RANS mode, e.g.,  $f_k = 1$ ,  $\Omega_\phi$  is independent of  $\Delta$  and should be modeled as  $\Omega_\phi = \Omega_{\phi_{\text{RANS}}} = C_{\phi_{\text{RANS}}} \Omega_{\text{RANS}} = C_{\phi_{\text{RANS}}} \beta^* \omega$ .
- (2) In VLES mode, e.g.,  $0.2 < f_k < 1$  and LES mode ( $0 < f_k \leq 0.2$ ),  $\Omega_\phi$  depends on  $\Delta$ , and is modeled as  $\Omega_\phi = \Omega_{\phi_{\text{LES}}} = C_{\phi_{\text{LES}}} \frac{v_t + v}{\Delta^2}$ .
- (3) In DNS mode, e.g.,  $f_k = 0$ ,  $\Omega_\phi$  is modeled as  $\Omega_\phi = \Omega_{\phi_{\text{DNS}}} = C_{\phi_{\text{DNS}}} \frac{v}{\Delta^2}$ .
- (4) During mode transition, (e.g.,  $f_k \rightarrow 0$  or  $f_k \rightarrow 1$ ), the spatial continuity in  $\Omega_\phi$  should be ensured.

The scalar-mixing rate model could be modified as follows:

$$\Omega_\phi = C_{\phi_{\text{hybrid}}} \frac{v_t + v}{L_{\text{hybrid}}^2} = \begin{cases} C_{\phi_{\text{RANS}}} \beta^* \omega & \text{if } f_k = 1 \\ C_{\phi_{\text{LES}}} \frac{v_t + v}{\Delta^2} & \text{if } 0 \leq f_k < 1 \end{cases} \quad (\text{A16})$$

TABLE I. Parameters and model variations for parametric studies in SATES-FDF simulations.

	$C_{\phi_{\text{RANS}}}$	$C_{\text{VLES}}$	Mixing model	Mixing-frequency model
Case 1	10	0.61	IEM	RANS-MFM
Case 2	10	0.61	IEM	LES-MFM
Case 3	10	0.61	IEM	Hybrid-MFM
Case 4	50	0.61	IEM	RANS-MFM
Case 5	50	0.61	IEM	LES-MFM
Case 6	50	0.61	IEM	Hybrid-MFM
Case 7	30	0.12	IEM	RANS-MFM
Case 8	30	0.12	IEM	LES-MFM
Case 9	30	0.12	IEM	Hybrid-MFM
Case 10	30	1.0	IEM	RANS-MFM
Case 11	30	1.0	IEM	LES-MFM
Case 12	30	1.0	IEM	Hybrid-MFM
Case 13	30	0.61	IEM	Hybrid-MFM
Case 14	30	0.61	MC	Hybrid-MFM
Case 15	30	0.61	EMST	Hybrid-MFM

To ensure the spatial continuity from LES-VLES mode to RANS mode,  $C_{\phi_{\text{RANS}}}$  and  $C_{\phi_{\text{LES}}}$  are correlated with  $C_{\phi_{\text{RANS}}} \beta^* \omega = C_{\phi_{\text{LES}}} \frac{\nu_t}{\Delta^2}$ , when  $f_k$  is exactly 1. Then, we assume that the  $k-\omega$  SST model is identical to the standard Smagorinsky LES model, which is similar to Johansen *et al.* [47], who did the same assumption on the standard  $k-\varepsilon$  model when  $f_k$  is exactly 1. Therefore,  $\nu_t = (C_S \Delta)^2 |S|$ . Besides, the governing equation of  $\omega$  in SST could be simplified by dropping the diffusion terms and unsteady term,

$$0 = \gamma \frac{\omega}{k} \bar{\rho} P_k - \beta_1 \bar{\rho} \omega^2. \quad (\text{A17})$$

Thus,  $\omega^2 = \gamma |S|^2 / \beta_1$ , and finally we get  $\frac{C_{\phi_{\text{LES}}}}{C_{\phi_{\text{RANS}}}} = \frac{\beta^* \sqrt{\frac{\gamma}{\beta_1}}}{C_S^2} = 0.24 / C_S^2$ . When  $C_S$  is set to 0.1,  $\frac{C_{\phi_{\text{LES}}}}{C_{\phi_{\text{RANS}}}} = 24$ . When  $f_k$  is exactly equal to 0,  $\nu_t = 0$ , left continuity is also naturally satisfied by  $\frac{C_{\phi_{\text{LES}}}}{C_{\phi_{\text{DNS}}}} = 1$ . The difference of  $\frac{C_{\phi_{\text{LES}}}}{C_{\phi_{\text{RANS}}}}$  between general HRLM-FDF and SATES-FDF is because the parameter  $C_{\text{VLES}} = 0.61$  is obtained by the assumption that the standard  $k-\varepsilon$  model aligns precisely with the standard Smagorinsky LES model when  $F_r$  equals 1, but in this section  $k-\omega$  SST model was used for derivation.

Or, if assuming that the  $k-\omega$  SST model is identical to the standard WALE LES model [73] when  $f_k$  is exactly 1, similarly, we can get  $\frac{C_{\phi_{\text{LES}}}}{C_{\phi_{\text{RANS}}}} = \frac{\beta^* \sqrt{\frac{\gamma}{\beta_1}}}{C_w^2} \cdot \frac{|S|}{S_w}$ , where  $S_w = \frac{(S_{ij}^d S_{ij}^d)^{1.5}}{(\bar{S}_{ij} \bar{S}_{ij})^{2.5} + (S_{ij}^d S_{ij}^d)^{1.25}}$ , and  $S_{ij}^d = \frac{1}{2} [(\frac{\partial \bar{u}_i}{\partial x_j})^2 + (\frac{\partial \bar{u}_j}{\partial x_i})^2] - \frac{1}{3} \delta_{ij} (\frac{\partial \bar{u}_k}{\partial x_k})^2$ .

### 3. Sensitivity of the parameters $C_{\phi_{\text{RANS}}}$ and $C_{\text{VLES}}$ and mixing model in SATES-FDF simulations

Fifteen cases, as outlined in Table I, were simulated. The results of mean temperature ( $T$ )–equivalence ( $\phi$ )–mass fraction of  $\text{CO}_2$  are shown in Fig. 15, which reveals that adjusting parameters  $C_{\phi_{\text{RANS}}}$  and  $C_{\text{VLES}}$  was ineffectual in improving the experimental conformity of predictions for RANS-MFM and LES-MFM. Significantly, hybrid-MFM consistently yielded predictions more in accord with experimental observations, surpassing the accuracy of both RANS-MFM and LES-MFM.

#### 4. Delayed Detached Eddy Simulation (DDES)-FDF simulations

Three cases, as outlined in Table II, were simulated. The results of mean temperature ( $T$ )–equivalence ( $\phi$ )–mass fraction of  $\text{CO}_2$  simulated by DDES-FDF are shown in Fig. 16. DDES-FDF and SATES FDF have similar results in the mixed-frequency model, where Hybrid-MFM get a better agreement with experimnt than RANS-MFM or LES-MFM.

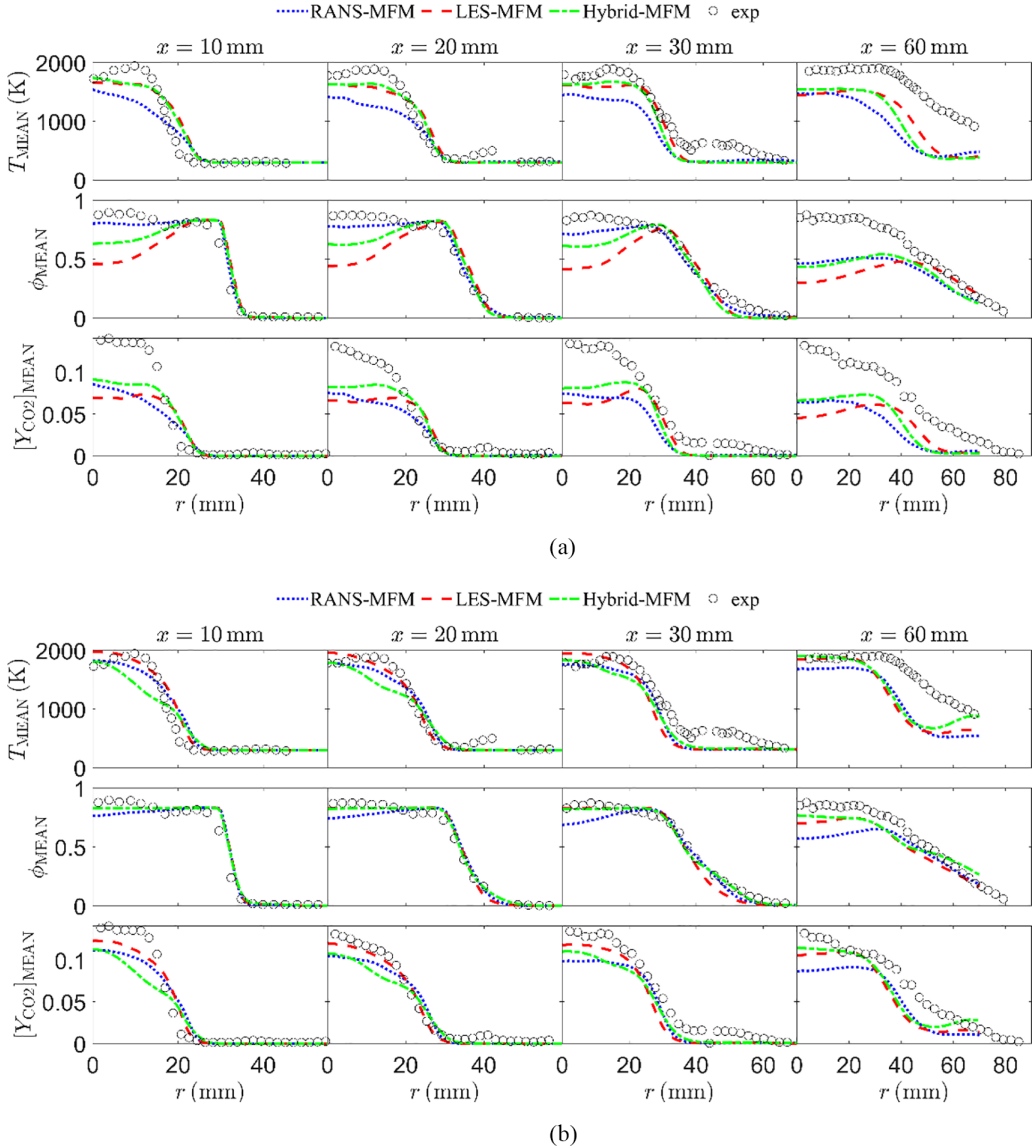
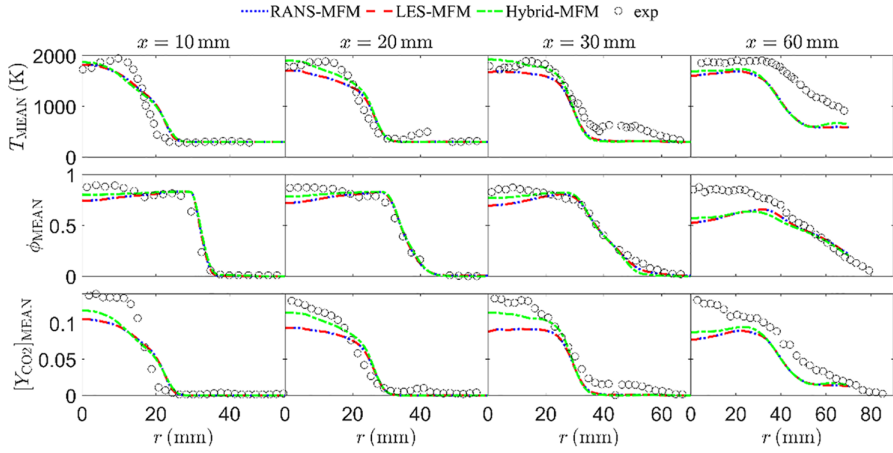
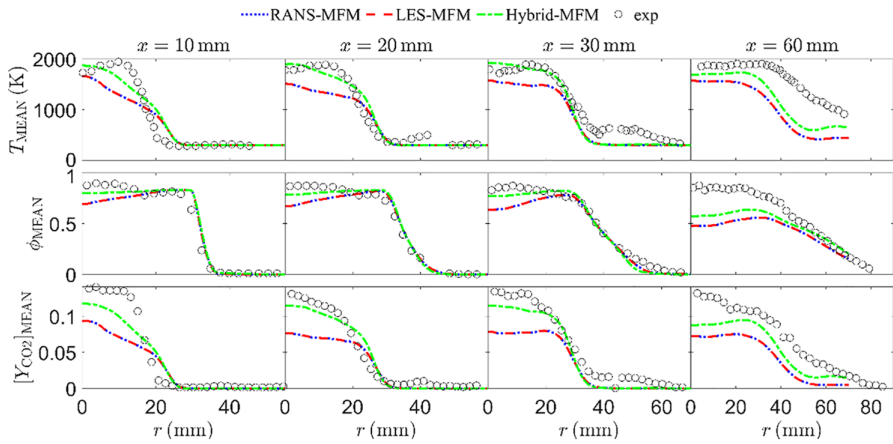


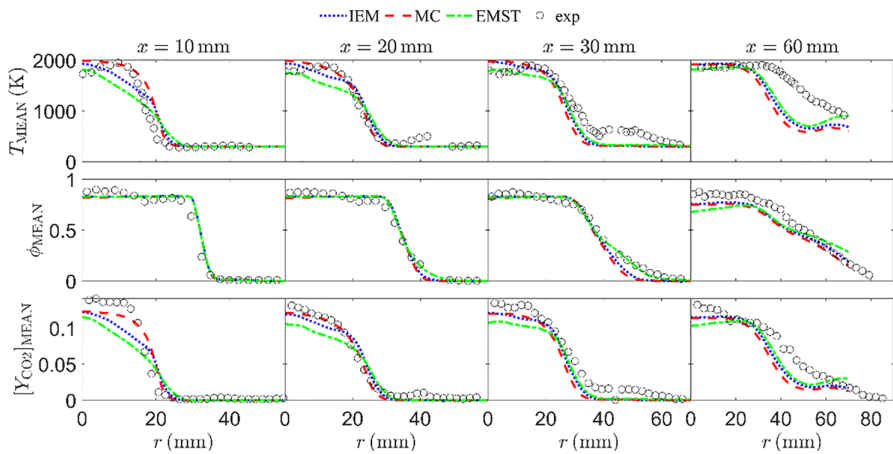
FIG. 15. Radial profiles of the mean temperature ( $T$ )–equivalence ( $\phi$ )–mass fraction of  $\text{CO}_2$  of the reacting case simulated by SATES-FDF. The profiles are shown at four axial positions ( $x = 10, 20, 30,$  and  $60$  mm). The symbols represent the experimental data [39] and the lines of different colors represent the simulation results with different methods, (a) Case 1 & Case 2 & Case 3, (b) Case 4 & Case 5 & Case 6.



(c)



(d)



(e)

FIG. 15. (Continued.) (c) Case 7 & Case 8 & Case 9, (d) Case 10 & Case 11 & Case 12, (e) Case 13 & Case 14 & Case 15.

TABLE II. Model variations for parametric studies in DDES-FDF simulations.

	$C_{\phi_{\text{RANS}}}$	$C_{\text{VLES}}$	Mixing model	Mixing-frequency model
Case 16	30	0.61	IEM	RANS-MFM
Case 17	30	0.61	IEM	LES-MFM
Case 18	30	0.61	IEM	Hybrid-MFM

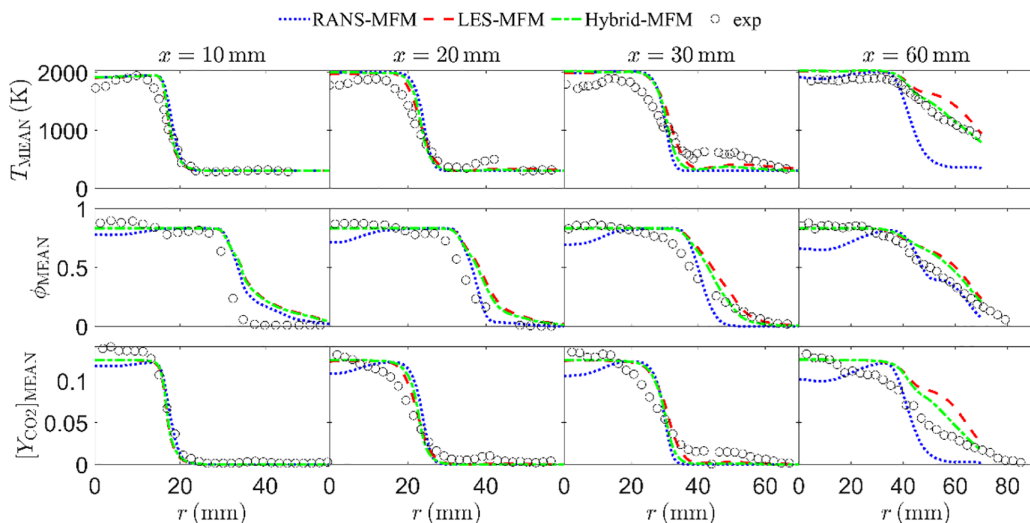


FIG. 16. Radial profiles of the mean temperature ( $T$ )–equivalence ( $\phi$ )–mass fraction of  $\text{CO}_2$  of the reacting case simulated by DDES-FDF. The profiles are shown at four axial positions ( $x = 10, 20, 30$  and  $60$  mm). The symbols represent the experimental data [39] and the lines of different color represent the simulation results with different methods, Case 16 & Case 17 & Case 18.

- [1] H. Pitsch, Large-eddy simulation of turbulent combustion, *Annu. Rev. Fluid Mech.* **38**, 453 (2006).
- [2] M. Ihme and H. Pitsch, Prediction of extinction and reignition in nonpremixed turbulent flames using a flamelet/progress variable model: 2. Application in LES of Sandia flames D and E, *Combust. Flame* **155**, 90 (2008).
- [3] Y. Ge, M. Cleary, and A. Klimenko, A comparative study of Sandia flame series (D–F) using sparse-Lagrangian MMC modelling, *Proc. Combust. Inst.* **34**, 1325 (2013).
- [4] M. Nik, S. Yilmaz, P. Givi, M. Sheikhi, and S. B. Pope, Simulation of Sandia flame D using velocity-scalar filtered density function, *AIAA J.* **48**, 1513 (2010).
- [5] M. Sheikhi, T. Drozda, P. Givi, F. Jaberri, and S. B. Pope, Large eddy simulation of a turbulent nonpremixed piloted methane jet flame (Sandia Flame D), *Proc. Combust. Inst.* **30**, 549 (2005).
- [6] H. Turkeri, X. Zhao, S. B. Pope, and M. Muradoglu, Large eddy simulation/probability density function simulations of the Cambridge turbulent stratified flame series, *Combust. Flame* **199**, 24 (2019).
- [7] H. Koo, P. Donde, and V. Raman, LES-based Eulerian PDF approach for the simulation of scramjet combustors, *Proc. Combust. Inst.* **34**, 2093 (2013).
- [8] W. Jones, A. Marquis, and V. Prasad, LES of a turbulent premixed swirl burner using the Eulerian stochastic field method, *Combust. Flame* **159**, 3079 (2012).

- [9] H. Wang and S. B. Pope, Large eddy simulation/probability density function modeling of a turbulent  $\text{CH}_4/\text{H}_2/\text{N}_2$  jet flame, *Proc. Combust. Inst.* **33**, 1319 (2011).
- [10] A. Kempf, R. Lindstedt, and J. Janicka, Large-eddy simulation of a bluff-body stabilized nonpremixed flame, *Combust. Flame* **144**, 170 (2006).
- [11] H. Zhou, Z. Ren, D. H. Rowinski, and S. B. Pope, Filtered density function simulations of a near-limit turbulent lean premixed flame, *J. Propuls. Power* **36**, 381 (2020).
- [12] P. Wolf, G. Staffelbach, A. Roux, L. Gicquel, T. Poinsot, and V. Moureau, Massively parallel LES of azimuthal thermo-acoustic instabilities in annular gas turbines, *C. R. Mecanique* **337**, 385 (2009).
- [13] N. Ansari, P. Piscuineri, P. Strakey, and P. Givi, Scalar-filtered mass-density-function simulation of swirling reacting flows on unstructured grids, *AIAA J.* **50**, 2476 (2012).
- [14] X. Zhao, D. Haworth, T. Ren, and M. Modest, A transported probability density function/photon Monte Carlo method for high-temperature oxy-natural gas combustion with spectral gas and wall radiation, *Combust. Theory Model.* **17**, 354 (2013).
- [15] S. Undapalli, S. Srinivasan, and S. Menon, LES of premixed and non-premixed combustion in a stagnation point reverse flow combustor, *Proc. Combust. Inst.* **32**, 1537 (2009).
- [16] S. T. Bose and G. I. Park, Wall-modeled large-eddy simulation for complex turbulent flows, *Annu. Rev. Fluid Mech.* **50**, 535 (2018).
- [17] P. R. Spalart, Strategies for turbulence modelling and simulations, *Int. J. Heat Fluid Flow* **21**, 252 (2000).
- [18] P. R. Spalart, Detached-eddy simulation, *Annu. Rev. Fluid Mech.* **41**, 181 (2009).
- [19] H. Foroutan and S. Yavuzkurt, A partially-averaged Navier–Stokes model for the simulation of turbulent swirling flow with vortex breakdown, *Int. J. Heat Fluid Flow* **50**, 402 (2014).
- [20] B. Basara, S. Krajnovic, S. Girimaji, and Z. Pavlovic, Near-wall formulation of the partially averaged Navier Stokes turbulence model, *AIAA J.* **49**, 2627 (2011).
- [21] S. Lakshminpathy and S. S. Girimaji, Partially averaged Navier–Stokes (PANS) method for turbulence simulations: Flow past a circular cylinder, *J. Fluids Eng.* **132**, 121202 (2010).
- [22] R. Schiestel and A. Dejoan, Towards a new partially integrated transport model for coarse grid and unsteady turbulent flow simulations, *Theor. Comput. Fluid Dyn.* **18**, 443 (2005).
- [23] X. Han and S. Krajnović, An efficient very large eddy simulation model for simulation of turbulent flow, *Int. J. Numer. Methods Fluids* **71**, 1341 (2013).
- [24] X. Han and S. Krajnović, Very-large-eddy simulation based on  $k-\omega$  model, *AIAA J.* **53**, 1103 (2015).
- [25] C. G. Speziale, Turbulence modeling for time-dependent RANS and VLES: A review, *AIAA J.* **36**, 173 (1998).
- [26] X. Han and S. Krajnović, Validation of a novel very large eddy simulation method for simulation of turbulent separated flow, *Int. J. Numer. Methods Fluids* **73**, 436 (2013).
- [27] Z. Xia, X. Han, and J. Mao, Assessment and validation of very-large-eddy simulation turbulence modeling for strongly swirling turbulent flow, *AIAA J.* **58**, 148 (2020).
- [28] Z. Xia, H. Zhang, X. Han, and Z. Ren, Self-adaptive turbulence eddy simulation of a premixed jet combustor, *Phys. Fluids* **35**, 085137 (2023).
- [29] S. B. Pope, Small scales, many species and the manifold challenges of turbulent combustion, *Proc. Combust. Inst.* **34**, 1 (2013).
- [30] S. Sammak, Z. Ren, and P. Givi, Modern developments in filtered density function, in *Modeling and Simulation of Turbulent Mixing and Reaction: For Power, Energy and Flight* (Springer, Singapore, 2020), p. 181.
- [31] D. C. Haworth, Progress in probability density function methods for turbulent reacting flows, *Prog. Energy Combust. Sci.* **36**, 168 (2010).
- [32] S. B. Pope, PDF methods for turbulent reactive flows, *Prog. Energy Combust. Sci.* **11**, 119 (1985).
- [33] P. Givi, Filtered density function for subgrid scale modeling of turbulent combustion, *AIAA J.* **44**, 16 (2006).
- [34] J. Villermaux and J.-C. Devillon, Représentation de la redistribution des domaines de ségrégation dans un fluide par un modèle d’interaction phénoménologique, in *Proceedings of the Second International Symposium on Chemical Reaction Engineering* (Elsevier, Amsterdam, 1972), pp. 1–13.
- [35] R. L. Curl, Dispersed phase mixing: I. Theory and effects in simple reactors, *AIChE J.* **9**, 175 (1963).

- [36] S. Subramaniam and S. B. Pope, A mixing model for turbulent reactive flows based on Euclidean minimum spanning trees, *Combust. Flame* **115**, 487 (1998).
- [37] Z. Ren and S. B. Pope, An investigation of the performance of turbulent mixing models, *Combust. Flame* **136**, 208 (2004).
- [38] H. Zhou, Z. Ren, M. Kuron, T. Lu, and J. H. Chen, Investigation of reactive scalar mixing in transported PDF simulations of turbulent premixed methane-air Bunsen flames, *Flow Turbul. Combust.* **103**, 667 (2019).
- [39] M. A. Gregor, F. Seffrin, F. Fuest, D. Geyer, and A. Dreizler, Multi-scalar measurements in a premixed swirl burner using 1D Raman/Rayleigh scattering, *Proc. Combust. Inst.* **32**, 1739 (2009).
- [40] A. Nauert, P. Petersson, M. Linne, and A. Dreizler, Experimental analysis of flashback in lean premixed swirling flames: Conditions close to flashback, *Exp. Fluids* **43**, 89 (2007).
- [41] C. Schneider, A. Dreizler, and J. Janicka, Fluid dynamical analysis of atmospheric reacting and isothermal swirling flows, *Flow Turbul. Combust.* **74**, 103 (2005).
- [42] D. Butz, Y. Gao, A. M. Kempf, and N. Chakraborty, Large eddy simulations of a turbulent premixed swirl flame using an algebraic scalar dissipation rate closure, *Combust. Flame* **162**, 3180 (2015).
- [43] M. Freitag and M. Klein, Direct numerical simulation of a recirculating, swirling flow, *Flow Turbul. Combust.* **75**, 51 (2005).
- [44] G. Kuenne, A. Ketelheun, and J. Janicka, LES modeling of premixed combustion using a thickened flame approach coupled with FGM tabulated chemistry, *Combust. Flame* **158**, 1750 (2011).
- [45] S. B. Pope, Ten questions concerning the large-eddy simulation of turbulent flows, *New J. Phys.* **6**, 35 (2004).
- [46] K. J. Hsieh, F.-S. Lien, and E. Yee, Towards a unified turbulence simulation approach for wall-bounded flows, *Flow Turbul. Combust.* **84**, 193 (2010).
- [47] S. T. Johansen, J. Wu, and W. Shyy, Filter-based unsteady RANS computations, *Int. J. Heat Fluid Flow* **25**, 10 (2004).
- [48] S. B. Pope, *Turbulent Flows* (Cambridge University Press, Cambridge, UK, 2000).
- [49] J. B. Perot and J. Gadebusch, A self-adapting turbulence model for flow simulation at any mesh resolution, *Phys. Fluids* **19**, 11 (2007).
- [50] M. Germano, Properties of the hybrid RANS/LES filter, *Theor. Comput. Fluid Dyn.* **17**, 225 (2004).
- [51] S. Viswanathan, H. Wang, and S. B. Pope, Numerical implementation of mixing and molecular transport in LES/PDF studies of turbulent reacting flows, *J. Comput. Phys.* **230**, 6916 (2011).
- [52] S. B. Pope, A model for turbulent mixing based on shadow-position conditioning, *Phys. Fluids* **25**, 110803 (2013).
- [53] T. Yang, Q. Xie, H. Zhou, and Z. Ren, On the modeling of scalar mixing timescale in filtered density function simulation of turbulent premixed flames, *Phys. Fluids* **32**, 115130 (2020).
- [54] A. Sirivat and Z. Warhaft, The effect of a passive cross-stream temperature gradient on the evolution of temperature variance and heat flux in grid turbulence, *J. Fluid Mech.* **128**, 323 (1983).
- [55] X. Wang, J. Wei, X. Su, H. Zhou, and Z. Ren, Investigation of reaction-induced subgrid scalar mixing in LES/FDF simulations of turbulent premixed flames, *Phys. Rev. Fluids* **7**, 124603 (2022).
- [56] H. Zhou, S. Li, Z. Ren, and D. H. Rowinski, Investigation of mixing model performance in transported PDF calculations of turbulent lean premixed jet flames through Lagrangian statistics and sensitivity analysis, *Combust. Flame* **181**, 136 (2017).
- [57] P. J. Colucci, F. A. Jaber, P. Givi, and S. B. Pope, Filtered density function for large eddy simulation of turbulent reacting flows, *Phys. Fluids* **10**, 499 (1998).
- [58] F. A. Jaber, P. J. Colucci, S. James, P. Givi, and S. B. Pope, Filtered mass density function for large-eddy simulation of turbulent reacting flows, *J. Fluid Mech.* **401**, 85 (1999).
- [59] U. Schumann, Realizability of Reynolds-stress turbulence models, *Phys. Fluids* **20**, 721 (1977).
- [60] F. Archambeau, N. Méchitoua, and M. Sakiz, Code Saturne: A finite volume code for the computation of turbulent incompressible flows-Industrial applications, *Int. J. Numer Methods Fluids* **1**, 1 (2004).
- [61] J. P. Van Doormaal and G. D. Raithby, Enhancements of the SIMPLE method for predicting incompressible fluid flows, *Numer. Heat Tr.* **7**, 147 (1984).

- [62] P. P. Popov, H. Wang, and S. B. Pope, Specific volume coupling and convergence properties in hybrid particle/finite volume algorithms for turbulent reactive flows, *J. Comput. Phys.* **294**, 110 (2015).
- [63] H. Wang, P. P. Popov, and S. B. Pope, Weak second-order splitting schemes for Lagrangian Monte Carlo particle methods for the composition PDF/FDF transport equations, *J. Comput. Phys.* **229**, 1852 (2010).
- [64] P. P. Popov and S. B. Pope, Implicit and explicit schemes for mass consistency preservation in hybrid particle/finite-volume algorithms for turbulent reactive flows, *J. Comput. Phys.* **257**, 352 (2014).
- [65] H. Wang, H. Zhou, Z. Ren, and C. K. Law, Transported PDF simulation of turbulent CH<sub>4</sub>/H<sub>2</sub> flames under MILD conditions with particle-level sensitivity analysis, *Proc. Combust. Inst.* **37**, 4487 (2019).
- [66] V. S. Arpaci and P. S. Larsen, *Convection Heat Transfer* (Prentice-Hall, New York, 1984).
- [67] S. Mazumder and M. F. Modest, A stochastic Lagrangian model for near-wall turbulent heat transfer, *J. Heat Transfer* **119**, 46 (1997).
- [68] S. B. Pope, Computationally efficient implementation of combustion chemistry using in situ adaptive tabulation, *Combust. Theory Model.* **1**, 41 (1997).
- [69] C. Friess, R. Manceau, and T. B. Gatski, Toward an equivalence criterion for Hybrid RANS/LES methods, *Comput. Fluids* **122**, 233 (2015).
- [70] L. Davidson and C. Friess, A new formulation of  $\overline{fk}$  for the PANS model, *J. Turbul.* **20**, 322 (2019).
- [71] A. Fadai-Ghotbi, C. Friess, R. Manceau, T. B. Gatski, and J. Borée, Temporal filtering: A consistent formalism for seamless hybrid RANS–LES modeling in inhomogeneous turbulence, *Int. J. Heat Fluid Flow* **31**, 378 (2010).
- [72] S. Heinz, A review of hybrid RANS-LES methods for turbulent flows: Concepts and applications, *Prog. Aerosp. Sci.* **114**, 100597 (2020).
- [73] F. Nicoud and F. Ducros, Subgrid-scale stress modelling based on the square of the velocity gradient tensor, *Flow Turbul. Combust.* **62**, 183 (1999).